

**UNIVERSIDAD SAN FRANCISCO DE QUITO
USFQ**

Colegio de Ciencias e Ingenierías

**Design and application of advanced BiFeO₃
nano-materials for the photodegradation of
organic pollutants in wastewater systems**
Proyecto de Investigación

Adriana Lucía Morales Gutiérrez

Ingeniería Química

Trabajo de titulación presentado como requisito
para la obtención del título de Ingeniería Química

Quito, 16 de mayo de 2019

UNIVERSIDAD SAN FRANCISCO DE QUITO USFQ
COLEGIO DE CIENCIAS E INGENIERÍAS

HOJA DE CALIFICACIÓN
DE TRABAJO DE TITULACIÓN

**Design and application of advanced BiFeO₃ nano-materials for
the photodegradation of organic pollutants in wastewater
systems**

Adriana Lucía Morales Gutiérrez

Calificación:

Nombre del profesor, Título académico:

Thomas Cadenbach, Dr. rer. nat.

Firma del profesor:

Quito, 16 de mayo de 2019

Derechos de Autor

Por medio del presente documento certifico que he leído todas las Políticas y Manuales de la Universidad San Francisco de Quito USFQ, incluyendo la Política de Propiedad Intelectual USFQ, y estoy de acuerdo con su contenido, por lo que los derechos de propiedad intelectual del presente trabajo quedan sujetos a lo dispuesto en esas Políticas.

Asimismo, autorizo a la USFQ para que realice la digitalización y publicación de este trabajo en el repositorio virtual, de conformidad a lo dispuesto en el Art. 144 de la Ley Orgánica de Educación Superior.

Firma del estudiante: _____

Nombres y apellidos: Adriana Lucía Morales Gutiérrez

Código: 00123853

Cédula de Identidad: 0503690547

Lugar y fecha: Quito, 16 de mayo de 2019

AGRADECIMIENTOS

A la Universidad San Francisco de Quito por otorgarme beca completa durante estos 5 años, permitiéndome estudiar esta hermosa carrera.

A Thomas Cadenbach, Dr. rer. nat., quien me orientó de la mejor manera posible durante la realización de esta investigación con sus conocimientos y su calidad de persona. Por su paciencia, tiempo y confianza para la realización de esta investigación.

Al departamento de Ingeniería Ambiental, quienes me permitieron la realización de los experimentos de este proyecto en sus laboratorios y al departamento de Ingeniería Química quienes me formaron como profesional dándome las bases para el desarrollo de este proyecto. De manera especial a Daniela Almeida, José Álvarez, Andrea Landázuri y David Egas.

Al Departamento de Física de la Escuela Politécnica Nacional, especialmente a María José Benítez, Dr. rer. nat. Y Christian Santacruz, PhD, por su ayuda en la caracterización de los materiales. De igual forma al Laboratorio de Caracterización de Nanomateriales de la Escuela Politécnica del Ejército, especialmente a Alexis Debut, PhD por las mismas razones. Análisis que complementaron altamente la realización de este proyecto.

A mi querida Vevs. René, Payola y Marcelo, quienes formaron la persona que soy.

A Misael Real-Enríquez, por su amor, ayuda, paciencia, apoyo y por creer en mí siempre que yo no lo hice.

Resumen

Nanomateriales de BiFeO₃ fueron sintetizados en los poros de un molde mesoporoso ordenado de sílica, SBA-15, por medio de una técnica de *nano-casting*. Con el fin de obtener un producto puro altamente cristalino, los efectos de diferentes agentes ligantes, solventes, pH, proporciones molares y procedimientos de calcinación fueron analizados. Técnicas de caracterización como difracción de rayos-x, microscopía de transmisión electrónica, espectroscopía infrarroja y espectrometría de reflectancia UV-vis difusa fueron usadas para confirmar la morfología, estructura cristalina, pureza de fase y propiedades ópticas de los materiales. Se encontró que las mejores condiciones de síntesis consisten en ácido tartárico como agente ligante, un exceso de bismuto del 3% y acidificación de 2-metoxietanol con ácido nítrico como solvente. Además, se comprobó que los procedimientos de calcinación tienen un fuerte impacto en la pureza de fase del compuesto deseado. Aquí, un paso de calentamiento intermedio de 200 a 250°C y finalmente a una temperatura de calcinación de 500°C por 1 h permitieron la formación de BiFeO₃ casi puro, con la presencia de 1.7% de Bi₂O₃ como impureza. Al remover la matriz de sílica, las nanopartículas (NPs) de BiFeO₃ fueron de 14 nm con una banda de energía de 2.05 eV atribuyéndole una buena actividad fotocatalítica bajo la radiación de luz visible. La actividad fotocatalítica de los materiales sintetizados fueron estudiados en la fotodegradación de Rodamina B bajo radiación de luz visible. Aquí, un 93% de RhB fue degradada dentro de 4 horas. Además, una disminución del pH en los experimentos fotocatalíticos mejoraron la eficiencia de degradación, con 100% de degradación a pH 2 en menos de 2h.

Palabras clave: Rodamina B, ferrita de bismuto, *nano-casting*, SBA-15, fotocatalisis, luz visible.

Abstract

BiFeO₃ nano-materials were synthesized via a nano-casting technique in the pores of an ordered mesoporous silica template, SBA-15. In order to obtain a pure highly crystalline product, the influence of different complexing agents, solvents, pH, molar ratios and calcination procedures were analyzed. Characterization techniques such as powder X-Ray diffractometry, transmission electron microscopy, infrared spectroscopy and UV–vis diffuse reflectance spectrometry were used to confirm the morphology, crystalline structure, phase purity and optical properties of the materials. It was found that the best synthetic conditions include tartaric acid as a complexing agent, a Bi excess of 3%, and HNO₃ acidified 2-methoxyethanol as solvent. Furthermore, calcination procedure proved to have a strong impact on the phase purity of the desired compound. Here an intermediate heat step at 200 to 250°C and a final calcination temperature of 500°C for 1 hour allows the formation of mostly pure BiFeO₃ with the presence of 1.7% of Bi₂O₃ as impurity. Leaching of the silica matrix resulted in 14 nm BiFeO₃ nanoparticles (NPs) with a bandgap value of 2.05 eV giving the sample a potential photocatalytic activity under visible light. The photocatalytic activity of the synthesized materials was studied by the photodegradation of the organic dye Rhodamine B under visible light irradiation. Here a 93% of RhB degradation was observed within 4 h. Moreover, decreasing the pH of the photocatalytic experiments showed an improvement in the degradation efficiency, with 100% degradation at pH 2 in less than 2 h.

Keywords: Rhodamine B, bismuth ferrite, nano-casting, SBA-15, photocatalysis, visible light.

Content

| | |
|--|----|
| Resumen | 5 |
| Abstract | 6 |
| 1. Introduction | 10 |
| 2. Experimental Details | 15 |
| 2.1. Characterization techniques and equipment | 15 |
| 2.2. Synthesis of SBA-15 | 15 |
| 2.2.1. Materials for the synthesis of SBA-15 | 15 |
| 2.2.2. Procedure for the synthesis of SBA-15 | 16 |
| 2.3. Synthesis of BiFeO₃ nano-materials | 16 |
| 2.3.1. Materials for the Synthesis of BiFeO₃ by nano-casting | 16 |
| 2.3.2. Reaction regarding the impact of complexing agents | 17 |
| 2.3.3. Reactions regarding solvent effects | 17 |
| 2.3.4. Reactions regarding bismuth volatility | 18 |
| 2.3.5. Nano-casting reactions | 19 |
| 2.4. Photocatalytic experiments | 20 |
| 2.5. Reuse of the Catalyst | 22 |
| 3. Results and Discussion | 22 |
| 3.1. Characterization | 22 |
| 3.1.1. Characterization of SBA-15 by Power X-Ray diffraction | 22 |
| 3.1.3. Transmission Electron Microscopy | 31 |
| 3.2. UV-vis Absorption Spectroscopy | 32 |
| 3.3. Photocatalytic activity | 33 |
| 4. Conclusion | 44 |
| References | 46 |
| Appendix | 51 |

List of Tables

| | |
|--|----|
| Table 1. Calcination paths for reactions regarding to impact of complexing agents, solvent effects and bismuth volatility..... | 18 |
| Table 2. Calcination paths for nano-casting reactions (ncr). | 20 |
| Table 3. Photodegradation kinetic parameters and degradation percentage of RhB in presence of different BiFeO ₃ materials. | 38 |
| Table 4. Photodegradation kinetic parameters and degradation percentage of RhB in presence of BiFeO ₃ liberated nanoparticles at different pH..... | 44 |

List of Figures

| | |
|--|-------------------------------------|
| Figure 1. Reaction mechanism of the photocatalysis degradation of organic pollutants using semiconductors (Santillán, P., 2017). | 11 |
| Figure 2. Scheme of the nano-casting technique by wet impregnation method. | 14 |
| Figure 3. Experimental setup for photocatalytic experiments (Santillán, P., 2017)..... | 21 |
| Figure 4. X-Ray diffractogram of SBA-15. | 23 |
| Figure 5. X-Ray diffractograms when using different complexing agents. | 24 |
| Figure 6. X-Ray diffractograms of BiFeO ₃ using different solvents..... | 25 |
| Figure 7. X-Ray diffractograms of BiFeO ₃ -0, x% samples with equimolar, 2%, 3% and 5% of bismuth excess, calcined with intermediate temperatures. | 26 |
| Figure 8. X-Ray diffractograms of BiFeO ₃ -1, x% samples with equimolar, 2%, 3% and 5% of bismuth excess, calcined without intermediate temperatures. .. | 28 |
| Figure 9. X-Ray diffractograms of BiFeO ₃ T,t@SBA-15, 3% samples, calcined at different final temperatures and hours. | 29 |
| Figure 10. X-Ray diffractograms of BiFeO ₃ , 3% before and after the leaching process to remove the silica matrix. | Error! Bookmark not defined. |
| Figure 11. a) TEM images of sample BiFeO ₃ -0, 3% (upper) and b) BiFeO ₃ , 3%-L leached (bottom). | 31 |
| Figure 12. UV-vis spectrum of BiFeO ₃ , 3%-L, the inset shows bandgap plot for BiFeO ₃ , 3%-L nanoparticles. | 32 |
| Figure 13. Mechanism of the photocatalytic degradation of RhB (Soltani, T. and Entezari, M., 2013, Merka, O., et al, 2011). | 33 |
| Figure 14. UV-vis spectra of RhB in dependence of irradiation time on BiFeO ₃ , 3%-L leached nanoparticles at pH 3, the inset is the color change of RhB for the first and last sample. | 34 |

| | |
|---|----|
| Figure 15. Photocatalytic degradation efficiency of RhB in presence of BiFeO ₃ nano-materials. | 36 |
| Figure 16. Photocatalytic degradation kinetics of RhB in presence of different BiFeO ₃ nano-materials. | 37 |
| Figure 17. FT IR spectra of materials before and after being used for photocatalysis. | 40 |
| Figure 18. Photocatalytic degradation of RhB in two successive cycles on BiFeO ₃ , 3%-L leached nanoparticles. | 39 |
| Figure 19. Photocatalytic degradation of RhB on BiFeO ₃ , 3%-L leached nanoparticles at different pH. | 41 |
| Figure 20. RhB molecule interactions according to the pH medium a) protonation of RhB, b) deprotonation of RhB, zwitterion formation. | 42 |
| Figure 21. Photocatalytic degradation kinetics of RhB in presence of BiFeO ₃ , 3%-L leached nanoparticles at different pH. | 43 |
| Figure 22.a. Solution of RhB mixed with BiFeO ₃ under visible light irradiation. | 51 |
| Figure 23.a. Wavelength spectra of the photoreactor used to simulate the visible light. | 51 |
| Figure 24.a. Calibration curve of RhB applied to calculate the concentration of RhB. | 52 |
| Figure 25. a. Color of the solution after the photodegradation of RhB with Bi _{1.03} FeO ₃ leached nanoparticles at pH 2. | 52 |
| Figure 26. a. Bi _{1.03} FeO ₃ leached nanoparticles catalyst. | 53 |

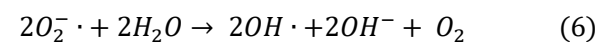
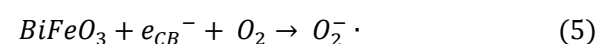
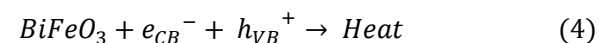
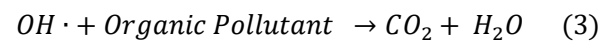
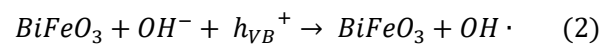
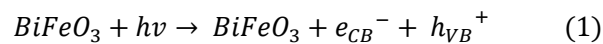
1. Introduction

Safe and readily available water is essential for public health (WHO, 2018). Although this necessity is well known, humanity as a whole faces increasing challenges and problems in providing clean and healthy water sources. Studies suggest that by 2025, half of the world's population will be living in water-stressed areas (WHO, 2018). Consequently, globally water-related crises are rising due to population growth, climate change, and environmental damage, making the scenario worse than ever particularly in low- and middle-income countries. Water pollution is one of the most challenging problems to face. For instance, more than 80% of the globally generated wastewater flows back into the environment untreated (UNESCO, 2017).

One of the most polluting industries is the textile industry, in which vast quantities of toxic and harmful organic and inorganic chemicals are utilized. The effluents resulting from this process contain residues of very stable and toxic dyes which cannot be treated by traditional methods used in wastewater treatment plants (Ghaly, A., et al, 2014). Techniques such as Advanced Oxidation Processes (AOP) showed advantages degrading dyes from wastewater effectively by completely mineralizing them in non-toxic substances like carbon dioxide (CO₂) and water (H₂O) (Mamun, Kurny, and Gulshan, 2015).

In this context, the design of semiconductor based-photocatalysis started a decade ago with the development of the first metal oxides catalysts such as titanium dioxide TiO₂ (Bhunia, et al., 2013, Gao, et al., 2006, Guo, et al., 2010). In general, the mechanism of a photocatalytic reaction requires an electron excitation from the valence band to the conduction band. The energy gap,

separating these bands is called bandgap. The excitation leads to the generation of an electron hole pair. The generated electron holes react with water to form hydroxyl radicals. Those radicals, which are strong oxidizing agents react with organic pollutants such as dyes, transforming them into carbon dioxide and water. Several parallel reactions can also occur once the electron hole pair is generated. First, a recombination of electrons and holes results in the production of thermal energy and a decrease in photoreaction efficiency. Second, the excited electrons can react with oxygen to generate superoxide anion which in turn can react with water, forming hydroxyl radical, hydroxide and molecular oxygen. The reaction steps are detailed in the following equations (Papadas, et al., 2013, 2014, Merka, et al., 2011, Reza, Kurny, and Gulshan, 2017).



These equations can be also seen in the following scheme with the mechanism of reaction.

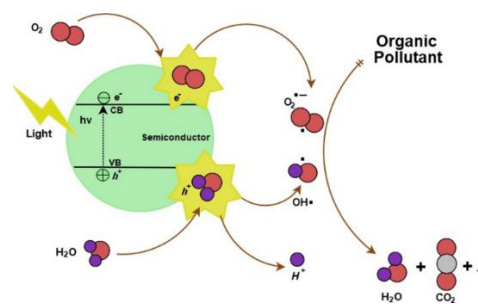


Figure 1. Reaction mechanism of the photocatalysis degradation of organic pollutants using semiconductors (Santillán, 2017).

Classic catalysts such as TiO₂, ZnO, SnO₂, among others, have been long studied to degrade these pollutants, but due to their large energy bandgap of ~3.2 eV, UV light is required in order to excite the electrons. This restricts their usage considering that only 4% of the sunlight contains UV light. Thus, practical applications are suffering from high costs and potentially hazardous equipment as UV light is cancerous (Bhunia, et al., 2013; Guo, et al., 2010). Therefore, the design and application of materials with low bandgaps, i.e. materials in which electron excitation can occur by absorbing visible light has been the focus of many research groups around globe. Bismuth ferrite (BiFeO₃) is one of those materials that has been largely researched in the past few years, since it has a narrow bandgap between 2.1 to 2.7 eV (Papadas, et al., 2013, 2014, Quiñonez, et al., 2013, Bhunia, et al., 2013). This allows complete mineralization of dyes such as Rhodamine B (RhB) or Methyl Orange (MO) molecules by absorbing visible light (Papadas, et al., 2013, 2014, Quiñonez, 2013; Bai, et al., 2016).

Since the photocatalytic degradation of organic molecules using a metal oxide photocatalyst is a heterogeneous process, it is obvious that efficiency and overall catalytic performance is strongly correlated to the number of active sites on the catalyst surface area and thus to particle size. Hence, the smaller the particle, the larger is the surface area and thus more active sites are available for photodegradation. In addition, it was shown that particle size and shape of BiFeO₃ has a direct influence in the bandgap of the corresponding material. Generally, smaller particles tend to have lower bandgaps than larger particles. (Reddy, et al., 2018, Quiñonez, et al., 2013, Bhunia, et al., 2013). Furthermore, calcination temperatures have shown to be also correlated with the energy bandgaps value, obtaining very small bandgaps of 1.7 eV at low calcination

temperatures (Pattnaik, et al., 2018). For those reasons, the development of BiFeO₃ nanomaterials and their corresponding application in photocatalysis has received an increasing attention over the last decade (Ponraj, Vinitha and Daniel, 2017).

However, the synthesis of pure single-phase BiFeO₃ is a difficult task, due to the volatile character of bismuth at temperatures higher than 500°C, which represents the required calcination temperature at which the material is formed (Lam, Sin and Rahman, 2017). This leads to the formation of undesired phases rich in iron and bismuth such as α -Fe₂O₃/Bi₂O₃ β -Bi₂O₃ or Bi₂Fe₄O₉. One way to overcome this obstacle is the in-situ formation of Fe/Bi mixed metal complexes by using different complexing agents such as carboxylic acids, which bind the metal precursors. During the calcination process the carboxylate ligands in the Fe/Bi complexes decompose while BiFeO₃ is being formed (Quiñonez, et al, 2013). Additionally, during the calcination particle growth and agglomeration can be observed (Bhunia, et al., 2013, Bai, et al., 2016) which consequently leads to larger particles. Thus, these high temperatures and long calcination times reduce the photocatalytic activity of the resulting material (Papadas, et al., 2013, 2014, Bhunia, et al., 2013, Quickel, et al., 2015). A proposed solution is to use a nanocasting technique also known as hard templating (Bai, et al., 2016, Gao, et al., 2006; Deng, et al., 2016). Here, synthesized mesoporous matrices act as rigid molds. After removal of the mold, the precursors are characterized by the negative replica structure with maximum particle diameter corresponding to the pore size of the porous matrix. Silica matrixes like Santa Barbara Amorphous silica type (SBA-15) or Korean Advanced Institute of Science and Technology

silica type (KIT-6) have been used successfully as hard templates to host metal oxide particles (Nair, et al, 2012, Deng, et al., 2016).

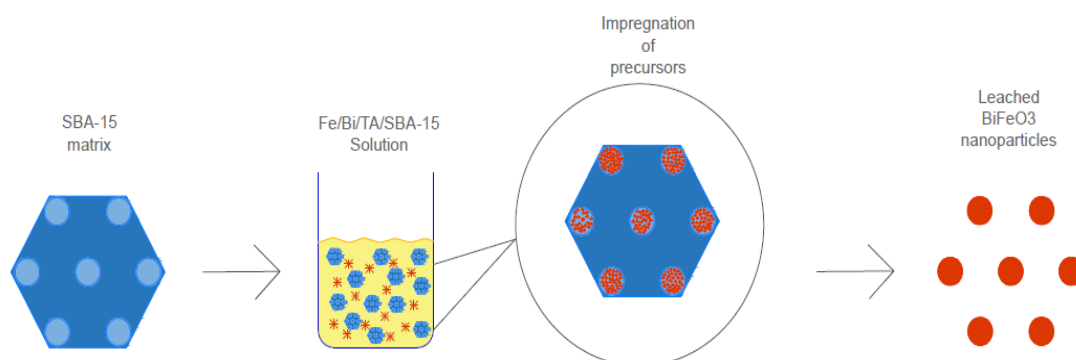


Figure 2. Scheme of the nano-casting technique by wet impregnation method.

This study focuses on the development of a highly crystalline pure-phase BiFeO_3 by determining the most suitable organic ligands, solvents, molar ratio of the precursors and calcination temperatures. Furthermore, using a wet impregnation of SBA-15, BiFeO_3 nanoparticles were synthesized in the mesopores of the silica matrix. By leaching of the silica matrix with sodium hydroxide (NaOH) liberated BiFeO_3 nanoparticles with a particle diameter corresponding to the pore size were obtained. The characterization techniques used to analyze these BiFeO_3 nano-materials are powder X-Ray diffraction (XRD), transmission electron microscopy (TEM), infrared spectroscopy and UV-visible reflectance spectroscopy.

Furthermore, the photocatalytic efficiency of this nano-material is analyzed in the photodegradation of RhB under various conditions, for instance under different pH conditions.

2. Experimental Details

2.1. Characterization techniques and equipment

Powder X-ray diffraction were recorded of the synthesized nano-materials to characterize its structure and phase purity with a PANalytical EMPYREAN diffractometer with a 2θ configuration (generator-detector) equipped with a Cu-tube ($\lambda=1.54 \text{ \AA}$) and a XCELERATOR detector and on a Bruker D2 Phaser equipped with a Cu-tube ($\lambda=1.54 \text{ \AA}$) and a LYNXEYE XE-T detector. Crystalline impurities were identified using MATCH! Phase Identification from Powder Diffraction. Transmission electron microscopic (TEM) images were recorded to analyze the particle size and morphology of the samples with a FEI Tecnai G2 spirit twin transmission electron microscope. Fourier transform infrared (FT IR) spectra of the nano-materials were recorded using a Jasco FT IR-4700 spectrometer. UV-visible diffuse reflectance spectra were recorded to obtain the bandgap value with a Perkin Elmer UV-vis spectrometer with an integrating sphere attachment. Spectra were suitably transformed by a Kubelka-Munk model in order to obtain the bandgap value (Kubelka and Munk, 1931). The absorption spectrum of RhB was measured using a UV-visible spectrophotometer GENESYS 30TM with a Tungsten-Halogen light source, and silicon photodiode detector. The spectra fittings were made with the Thermo Scientific VISIONlite PC software.

2.2. Synthesis of SBA-15

2.2.1. Materials for the synthesis of SBA-15

- Pluronic 123 (P123, Poly(ethylene glycol)-poly(propylene glycol)-poly(ethylene glycol) $M_{av} = 5800$, EO₂₀PO₇₀EO₂₀)

- Hydrochloric acid (HCl 37-38%)
- Deionized water
- Tetraethyl orthosilicate (TEOS, reagent grade, 98%)

All chemicals were used without further purification.

2.2.2. Procedure for the synthesis of SBA-15

The synthesis was performed by a slight modification of the published route (Deng, et al., 2016). For the preparation of 6.9 g of SBA-15 with a yield of 95%, first 13.9 g of P123, 252 g of deionized water and 7.7 g of HCl were dissolved in a polypropylene bottle (1000 mL). The solution was left under stirring for 4 hours at room temperature, until a homogeneous solution was obtained. After that time, the temperature was set to 35°C on a hot plate (crucial temperature to get the specific nano-porous size desired). When the temperature was reached, 25 g of TEOS was added, and the solution was left stirring for 24 hours. For complete condensation of the silica precursor a hydrothermal treatment was needed. For this, the bottle was put in an oven at 100°C for 24 hours. After this time, a white solid precipitated at the bottom of the bottle was found and was collected by vacuum filtration. This obtained product was dried in an oven at 90°C for 48 h. Finally, this powder was crushed and transferred to a crucible in order to be calcined.

2.3. Synthesis of BiFeO₃ nano-materials

The syntheses of BiFeO₃ nanoparticles were accomplished via a wet impregnation method.

2.3.1. Materials for the Synthesis of BiFeO₃ by nano-casting

- Iron nitrate [$\text{Fe}(\text{NO}_3)_3 \cdot 9\text{H}_2\text{O}$]
- Bismuth nitrate [$\text{Bi}(\text{NO}_3)_3 \cdot 5\text{H}_2\text{O}$]
- Tartaric acid (TA)
- Oxalic acid (OA)
- Nitric acid (HNO_3)
- 2-methoxyethanol (MetOH)
- Ethanol (EtOH)

2.3.2. Reaction regarding the impact of complexing agents

In order to study the influence of different complexing agents oxalic acid and tartaric acid were used. In a beaker 1.0148g or (2.5 mmol) of $\text{Fe}(\text{NO}_3)_3 \cdot 9\text{H}_2\text{O}$ and 1.2434g (2.56) mmol of $\text{Bi}(\text{NO}_3)_3 \cdot 5\text{H}_2\text{O}$ was weighted, then the organic acid, 0.2261g (2.5 mmol) of OA or of 0.3726g (2.5 mmol) TA was added. Here, 30 mL of 2M HNO_3 was being used as a solvent, obtaining a $\text{pH} < 4$. The solution was left stirring until a clear solution was observed followed by an evaporation using a rotary evaporator at 75°C . Then, the sample was dried in an oven at 75°C until a powder was obtained. Finally, the sample was calcined, the calcination specifications are detailed in Table 1.

2.3.3. Reactions regarding solvent effects

To analyze the effect of different solvents, ethanol and 2-methoxyethanol were tested in the synthesis. It should be noted that ethanol is commonly used in nano-casting syntheses. The experiment was performed as described in section 2.3.2., but here 30 mL of ethanol or 2-methoxyethanol respectively and 10 mL of HNO_3 were added in the syntheses as solvent. In the case of the reaction using ethanol, no nitric acid was added due to a potentially explosive reaction.

2.3.4. Reactions regarding bismuth volatility

As mentioned above, bismuth is rather volatile at temperatures > 400 °C. Thus, an excess bismuth is necessary to overcome bismuth loss during calcination. In order to study the influence of bismuth nitrate excess with respect to iron nitrate a series of reactions were performed using 4 different molar ratios between iron nitrate and bismuth nitrate. The first one with equimolar ratio, and the rest reactions with 2%, 3% and 5% excess of bismuth nitrate, respectively. The procedure continued as described in section 2.3.3., using 2-methoxyethanol as solvent, except for a variation in the calcination step.

Table 1. Calcination paths for reactions regarding to impact of complexing agents, solvent effects and bismuth volatility.

| Path | Reaction regarding: complexing agents, solvents, molar ratio-0 | Reaction regarding molar ratio-1 |
|--------------------------|--|--|
| Initial temperature (°C) | 25 | - |
| Heat rate 1 (°C/min) | 1 | - |
| Temperature 1 (°C) | 200 | - |
| Drying Time 2 (h) | 2 | - |
| Heat rate 2 (°C/min) | 1 | - |
| Temperature 2 (°C) | 250 | - |
| Drying Time 3 (h) | 2 | - |
| Heat rate 3 (°C/min) | 4 | 4 |
| Temperature 3 (°C) | 500 | 500 |
| Drying Time 3 (h) | 1 | 1 |

In order to study the effect of different calcination procedures with and without intermediate plateaus in the formation of undesired phases, the obtained powder was split into two parts. Both parts were calcined differently as it can be seen in Table 1. The different syntheses will be express as $BiFeO_3\text{-}\#$, $x\%$, where $\#$ is the path of calcination used and x is the bismuth excess.

2.3.5. Nano-casting reactions

To apply the nano-casting technique the experiment was performed as described in section 2.3.4., using 3% of bismuth nitrate excess, and then 0.7361g of SBA-15 was added. To allow a complete impregnation of the precursor inside the porous of the silica matrix, the solution was left stirring overnight. For these reactions a slow evaporation in the rotary evaporator was an important step to allow a complete impregnation.

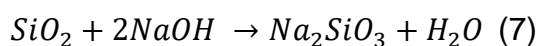
2.3.5.1. Calcination experiments for nano-casting reactions

The impact of different calcination paths was analyzed by varying calcination time and final calcination temperature due to their correlation with nanoparticle sizes and bandgap values (Pattnaik, et al, 2017, He, et al., 2013). Table 2 presents the calcination details of each sample. The final temperatures studied were 500°C and three different drying times, 600°C with two different drying times and 800°C for 1 h. These different syntheses will be express as $BiFeO_3 T,t@SBA-15, 3\%$, where T is the final calcination temperature and t is the time at which each sample was calcined at the final temperature.

Table 2. Calcination paths for nano-casting reactions (ncr).

| Nano-casting reactions | | | | | | |
|--------------------------|-------|-------|-------|-------|-------|-------|
| Path | ncr-1 | ncr-2 | ncr-3 | ncr-4 | ncr-5 | ncr-6 |
| Initial temperature (°C) | 25 | 25 | 25 | 25 | 25 | 25 |
| Heat rate 1 (°C/min) | 1 | 1 | 1 | 1 | 1 | 8 |
| Temperature 1 (°C) | 200 | 200 | 200 | 200 | 200 | - |
| Drying Time 2 (h) | 2 | 2 | 2 | 2 | 2 | - |
| Heat rate 2 (°C/min) | 1 | 1 | 1 | 1 | 1 | - |
| Temperature 2 (°C) | 250 | 250 | 250 | 250 | 250 | - |
| Drying Time 3 (h) | 2 | 2 | 2 | 2 | 2 | - |
| Heat rate 3 (°C/min) | 4 | 4 | 4 | 4 | 4 | - |
| Temperature 3 (°C) | 500 | 500 | 500 | 600 | 600 | 800 |
| Drying Time 3 (h) | 1 | 2 | 4 | 1 | 2 | 1 |

To eliminate the silica template and to obtain the BiFeO₃ NPs, a leaching process with a stoichiometric exact amount of 2 M NaOH based on the silica matrix was applied. The corresponding amount of NaOH required to remove the silica was calculated according to the following reaction.



The NaOH solution was split into two parts for two separate washings. After each washing the NaOH/BiFeO₃@SBA-15 mixture was left in the oven overnight at 75°C. After this, the sample was washed with deionized water and centrifuged until a pH of ~7 was reached.

2.4. Photocatalytic experiments

The photocatalytic activity of the samples was evaluated by the degradation of RhB in water at room-temperature under visible light. For this, a self-constructed

air-and water-cooled photoreactor equipped with high intensity LEDs with a spectral wavelength of 400-700nm, acted as a continuous sunlight simulator.

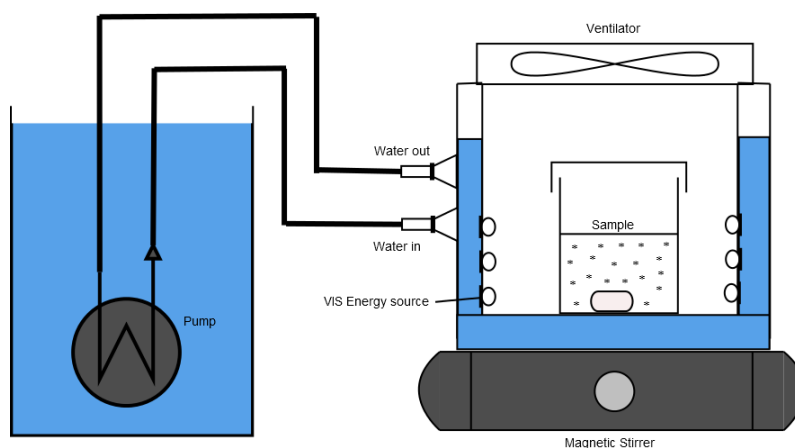


Figure 3. Experimental setup for photocatalytic experiments (Santillán, P., 2017).

For a typical run, 50 mL of dye solution (5mg/L) was mixed with 50 mg of BiFeO_3 sample and the mixture was stirred for 60 min in darkness, in order to reach an adsorption-desorption equilibrium between the catalyst, and the dye solution. After irradiation, aliquots were taken every 30 min and centrifuged to separate the catalyst. In order to calculate the concentration, the relation between intensity of the absorption peak and concentration according to the Beer-Lambert equation was determined as described in the following equation.

$$A = \log_{10} \frac{I_0}{I} = \epsilon l c \quad (8)$$

where A is absorption, I_0 is the initial intensity and I is intensity that passes through the sample, ϵ is the molar absorptivity coefficient ($\text{M}^{-1}\text{cm}^{-1}$), l is the path length (cm) and c is the sample concentration (M) (Bai, et al., 2016). A calibration curve based on the Beer-Lambert Law with 7 points was made. The linear equation to quantify the RhB concentration had a R^2 of 0.9959. Then, the

absorbance of each sample during photocatalysis was measured at the maximum absorption peak of RhB ($\lambda=555$ nm).

2.5. Reuse of the Catalyst

A series of reactions were executed in order to determine the reusability of the catalyst. For the first one 100 mL of RhB solution (5mg/L) was mixed with 100 mg of liberated nanoparticles of BiFeO₃, 3%-L. Then the same procedure described in the photocatalytic experiments section was carried out. After 4 hours, the BiFeO₃, 3% catalyst was separated from the solution and washed several times with deionized water by centrifugation. The recovered catalyst was re-activated by drying it at 75°C overnight, and then for the second experiment 50 mL of RhB solution was mixed with 50 mg recycled BiFeO₃, 3%.

3. Results and Discussion

3.1. Characterization

3.1.1. Characterization of SBA-15 by Power X-Ray diffraction

The synthesized SBA-15 powder was characterized by powder low angle X-Ray diffraction to guarantee the mesostructured and purity of the SBA-15. Figure 4 shows diffractogram of the sample, which exhibits a typical pattern of SBA-15. The peaks marked at these low-angle range between $2\theta = 1^\circ$ to 2° are reported to represent a typical highly ordered SBA-15 with hexagonal $p6mm$ structure (Huang, C., et al., 2010). Further, based on the protocol it is known that the SBA-15 synthesized at 100°C has a pore size of approximately 8 nm, and a surface area of about 700-750 m²/g (Deng, et al., 2016, Ishii, et al., 2013). Therefore, this

material was used for the impregnation experiments in this project as a hard template to cast BiFeO₃ nanoparticles.

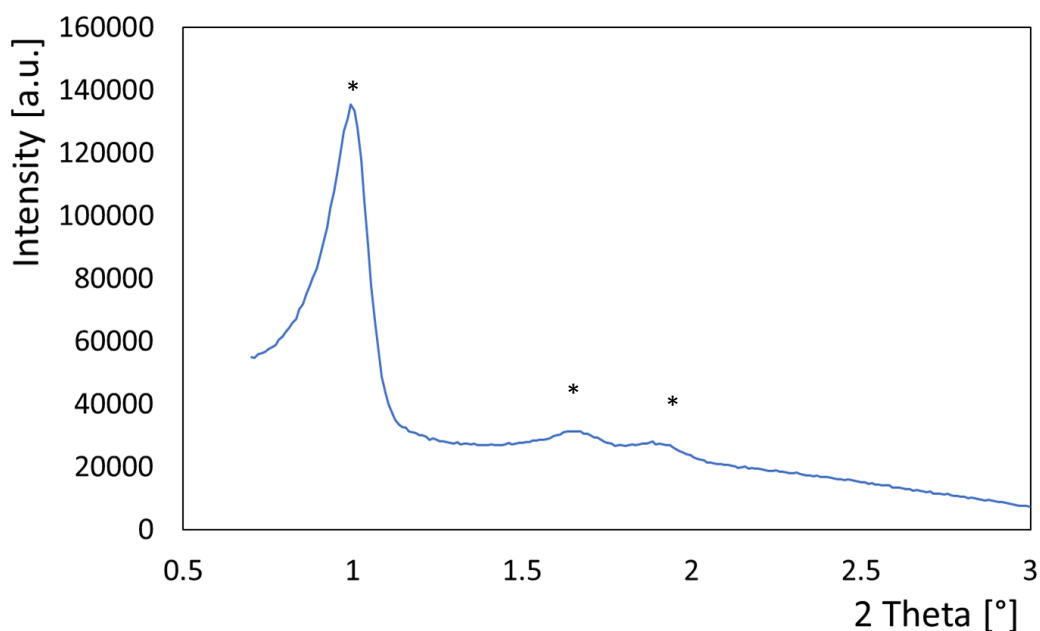


Figure 4. X-Ray diffractogram of SBA-15.

3.1.2. Characterization of BiFeO₃ samples by Power X-Ray diffraction

3.1.2.1. Effect of different complexing agents

In order to analyze the effect of different complexing agents, various organic acids (or.acs) were used in the synthesis of BiFeO₃. As described above, the formation of Bi/Fe/or.acs complexes occur, which keeps both metals in close proximity. After that, the drying step helps to eliminate solvents by evaporation and a powder is obtained. Finally, the calcination step, which is carried out at higher temperatures (~500°C), decompose these complexing agents, leaving Fe and Bi in proximity, forming BiFeO₃. However, the formation of impurities is often strongly correlated with metal-ligand interactions (Quiñonez, et al., 2013). Thus, from the powder X-Ray diffraction patterns shown in Figure 5 no formation of BiFeO₃ using oxalic acid and tartaric acid in the presence of nitric acid in a wet

impregnation method was observed. Most likely, the solvent/organic ligand combination in these reactions favored the reaction of the Lewis-acidic metals, in particular bismuth, with the SiO₂ of the hard template resulting in an amorphous product.

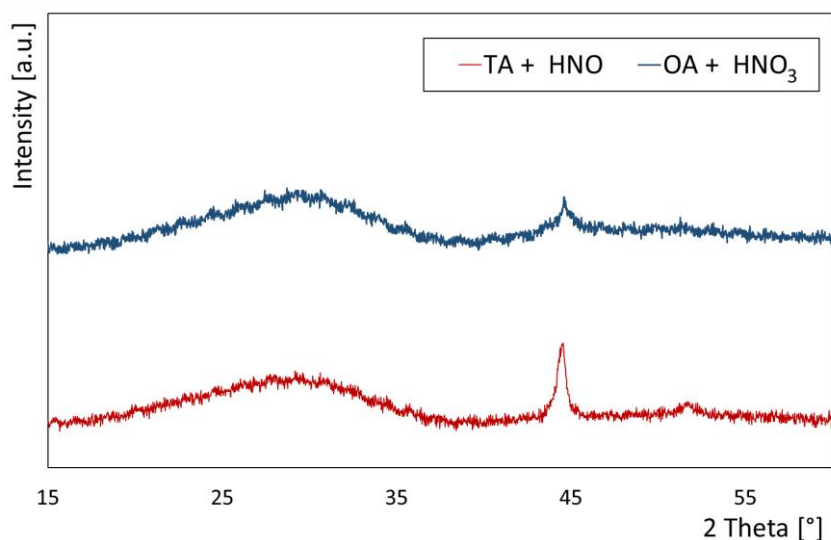


Figure 5. X-Ray diffractograms when using different complexing agents.

3.1.2.2. Effect of different solvents

The influence of different solvents during the synthesis was evaluated by using 2-methoxyethanol and ethanol. It should be noted that both solvents can interact with metal nitrates resulting into complex formation (Guo, et al., 2010). Figure 6 shows the differences between the diffractograms of the corresponding samples. Both samples followed the same procedure, but in the case of the reaction with ethanol, nitric acid was not added due to their chemical incompatibility, leading to a potentially explosive mixture. Analyzing the XRD data it becomes obvious that 2-methoxyethanol as solvent in combination with nitric acid showed better results in the formation of BiFeO₃. Approximately 50.5% of the crystalline products is BiFeO₃ as it can be seen in the diffractogram shown in Figure 6 (Lotey, G. S. and Verma, N. K., 2013). However, impurities present in the samples could be

identified at $2\theta = 27.85, 29.29, 31.61, 33.03, 45.55, 46.51, 51.61$ and 55.50° , which can be assigned to Bi_2O_3 (approx. 33%) and $\text{Bi}_2\text{O}_{2.7}$ (16.5%). The use of ethanol resulted primarily in the formation of Bi_2O_3 . While BiFeO_3 was formed when using 2-methoxyethanol, it is obvious that an improvement of the synthesis was essential.

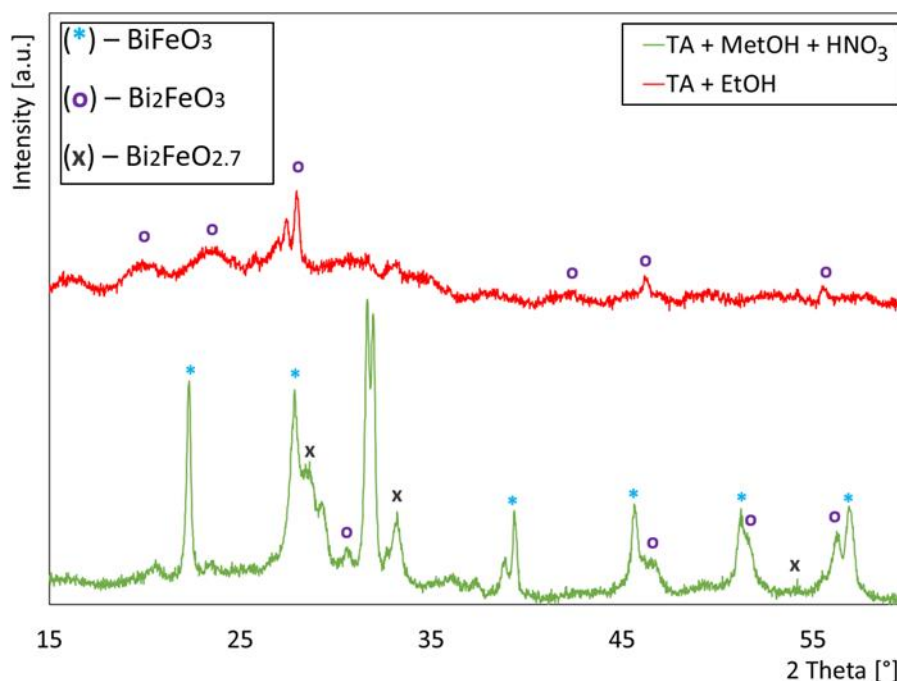


Figure 6. X-Ray diffractograms of BiFeO_3 using different solvents.

3.1.2.3. Effect of different molar ratio between metal precursors

The effect of different molar ratios between metal precursors was analyzed since bismuth is a volatile compound. Thus, it was necessary to overcome that loss during the heating step by adding an excess of bismuth. For this, the samples were carried out with equimolar ratio of iron and bismuth, and with 2, 3 and 5% of bismuth excess. Figure 7 shows the diffractograms with different molar ratios. The diffractograms show the impact of the molar ratio on the purity of the product. In general, all the diffractograms show that the samples with an excess of Bi have the reflection peaks which can be indexed as phase pure rhombohedral BiFeO_3

with a space group R3c, (JCPDS file no. 86-1518) according to reported data (Lotey, and Verma, 2013; Soltani and Entezari, 2013). For the equimolar reaction, the resulting BiFeO₃-0 diffractogram shows an impurity at $2\theta = 27.96$ which is 2.8% of Bi₂O₃ phase. Furthermore, all the diffractograms also show broad peaks indicating the formation of nanoparticles (Pattnaik, et al, 2017). However, the best molar ratio for the formation of BiFeO₃ was with 3% of Bi excess. The BiFeO₃-0, 3% diffractogram shows the representative peaks of pure highly crystalline BiFeO₃ and a broad peak at $2\theta = 32.10^\circ$ with a FWHM (Full Width at Half Maximum) of 0.3460° . Meanwhile, the peak of the BiFeO₃-0, 2% sample at the same angle has a FWHM of 0.3060° indicating the formation of more crystalline product compared to the other samples and favorable to the formation of bigger particles. (Reddy, Shekar, Park, 2018). The diffractogram of BiFeO₃-0, 5% shows similar results as BiFeO₃-0, 3%, however 5% of Bi excess is unnecessary to obtain the desired product.

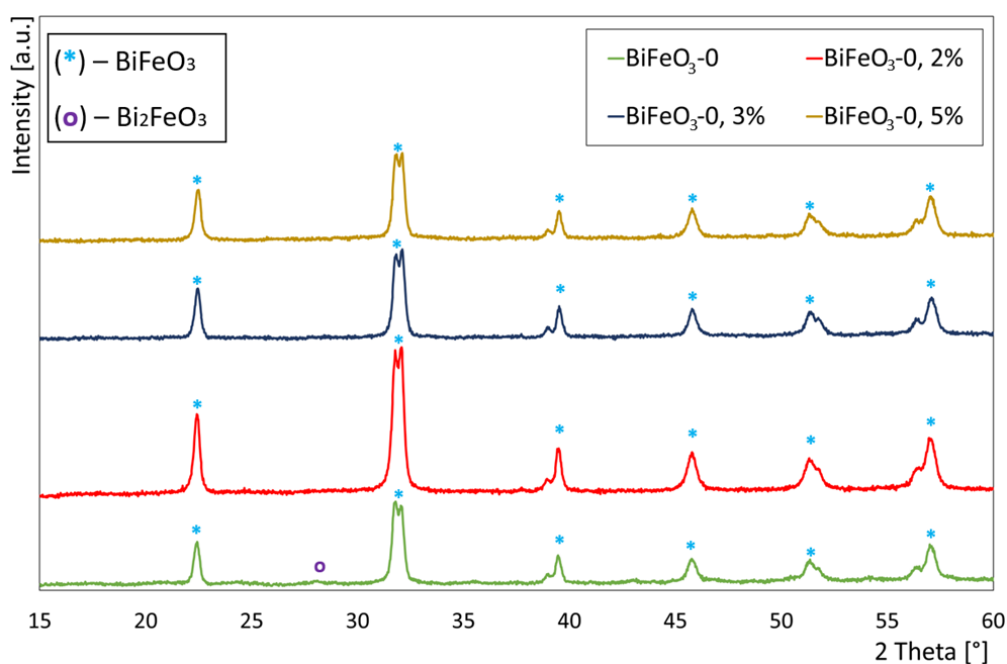


Figure 7. X-Ray diffractograms of BiFeO₃-0, x% samples with equimolar, 2%, 3% and 5% of bismuth excess, calcined with intermediate temperatures. (*) - BiFeO₃, (o) - Bi₂O₃

3.1.2.4. Influence of different calcination conditions

The influence of different calcination conditions was analyzed, especially when the calcination step does and does not have intermediate temperatures. For this, the samples of equimolar ratio and with 2, 3 and 5% of bismuth excess were split into two parts. Figure 7 shows the diffractograms of the half that was calcined with intermediate temperatures, and Figure 8 shows the diffractograms of the other half that was calcined directly at the final calcination temperature. Figure 8 shows that the diffractogram of the four samples display peaks which belong to rhombohedral BiFeO_3 phase. It should be noted that BiFeO_3 was formed by around 92, 75, 86, and 69% in these reactions with main impurities corresponding to Bi_2O_3 and $\text{Bi}_{25}\text{FeO}_{40}$ (Quiñonez, et al, 2013, Soltani and Entezari, 2013). The results shown in Figure 7 and 8 clearly show the strong correlation of the formation of pure single-phase BiFeO_3 and the applied calcination procedure. Here intermediate calcination plateaus help to decrease the formation of impurities. It should be noted that during the calcination, the presence of Bi (III) in acidic aqueous solutions leads to the formation of polynuclear cationic species. Once the thermal treatment at 500°C is applied, those clusters decompose into α - and β - Bi_2O_3 byproducts which are not observed with an intermediate heating step at 350°C (Quiñonez, et al, 2013). In this case, the temperature was hold at 200°C for 2 h, 250°C for 2h and finally at 500°C for 1h.

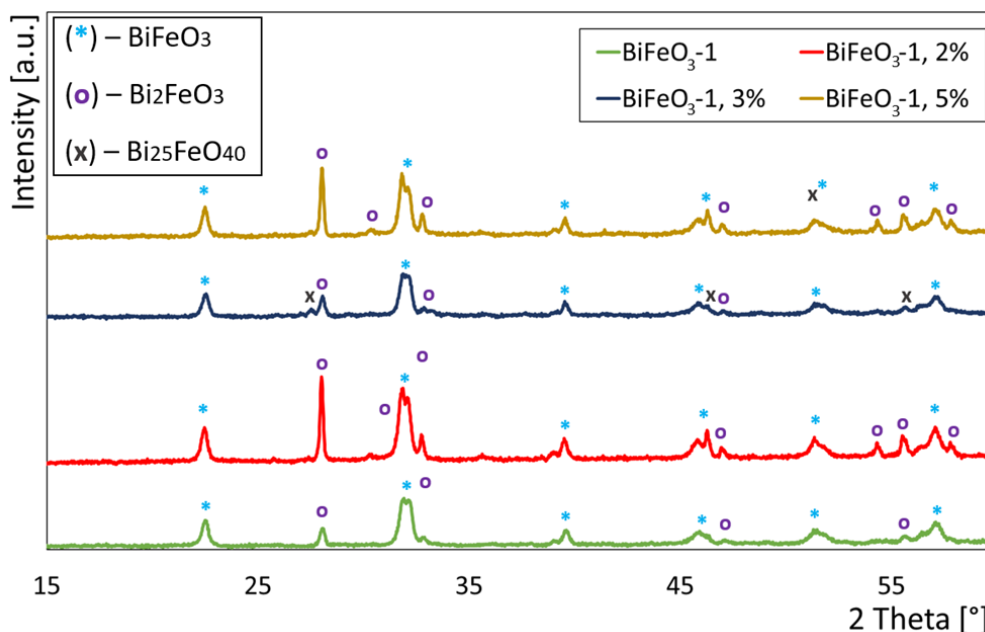


Figure 8. X-Ray diffractograms of BiFeO₃-1, x% samples with equimolar, 2%, 3% and 5% of bismuth excess, calcined without intermediate temperatures. (*), BiFeO₃; (o), Bi₂FeO₃; (x), Bi₂₅FeO₄₀

3.1.2.5. Synthesis of BiFeO₃ nanoparticles using SBA-15 as a hard template

Once the sample with 3% of Bi excess was selected as the best molar ratio for the formation of BiFeO₃, SBA-15 was added to the syntheses for the nano-casting technique. Furthermore, these samples were calcined at different final temperatures for different times to also analyze their effect in the formation of the catalyst within the pores of SBA-15. Figure 9 shows the diffractograms of the samples calcined at 500°C (1, 2 and 4 h), 600°C (1 and 2 h), and 800°C (1h). It should be noted that by increasing the final calcination temperature an increase in the formation of unwanted secondary phases is observed. These secondary phases for the samples calcined at 600°C mainly is Bi₂O₃ and for the samples calcined at 800°C mainly is Bi₂Fe₄O₉. Those impurities form due to Bi loss at calcination temperatures higher than ~500°C. When the temperature is kept at 500°C phase formation of BiFeO₃ is observed. Furthermore, all samples show a very broad peak between 2θ = 15° and 2θ = 35° indicating the presence of

amorphous SBA-15. The present results clearly show that phase pure formation of BiFeO_3 occur at low temperatures and short calcination time. It should be noted that at this temperature phase pure and highly crystalline BiFeO_3 is obtained. Thus, the sample BiFeO_3 500,1@SBA-15, 3% showed better characteristics for the present research.

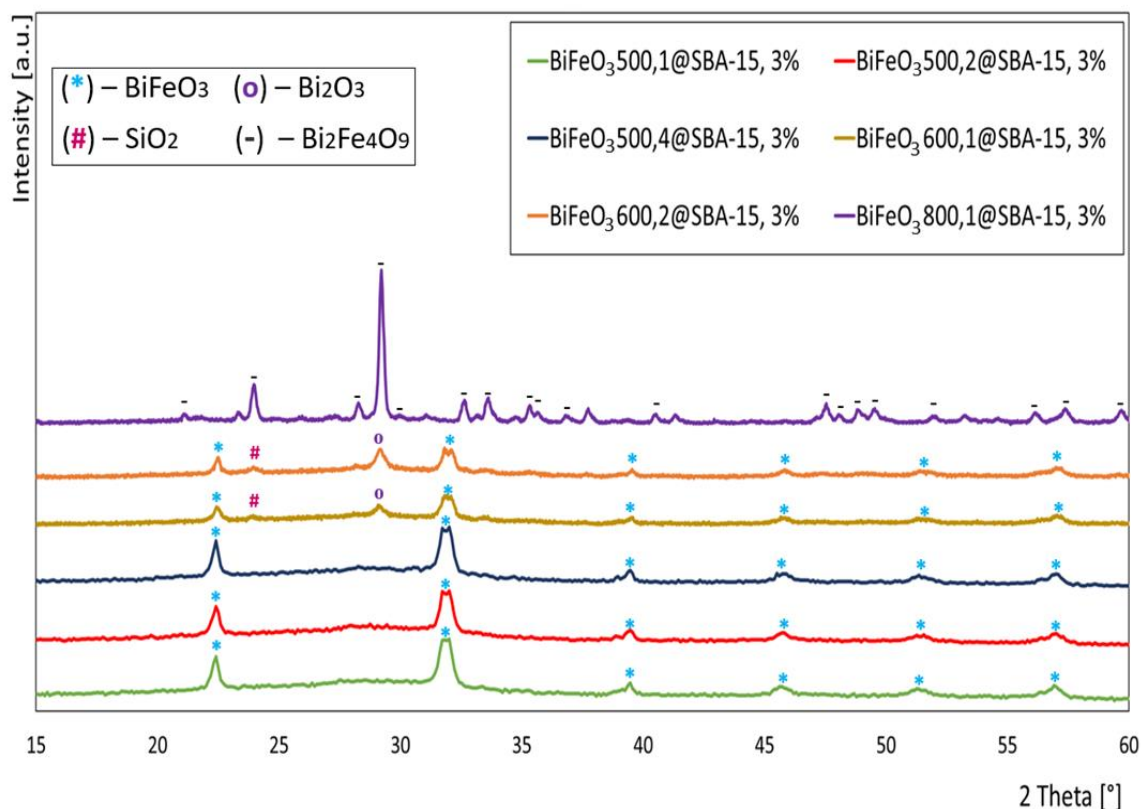


Figure 9. X-Ray diffractograms of BiFeO_3 T,t@SBA-15, 3% samples, calcined at different final temperatures and hours.

3.1.2.6. Leaching process to liberate BiFeO_3 nanoparticles from the silica matrix

After the identification of phase purity, BiFeO_3 500,1/SBA-15, 3% was leached with NaOH in order to liberate the nano-casted material. Figure 10 shows the pattern of BiFeO_3 , 3%-L, after the removal of the silica matrix. Here, a minor impurity corresponding to 1.7% of Bi_2O_3 is shown in the diffractogram which could not be detected prior due to the overlapping of a very broad peak coming of

amorphous SBA-15. However, the sample consists of 98.3% of highly crystalline BiFeO₃.

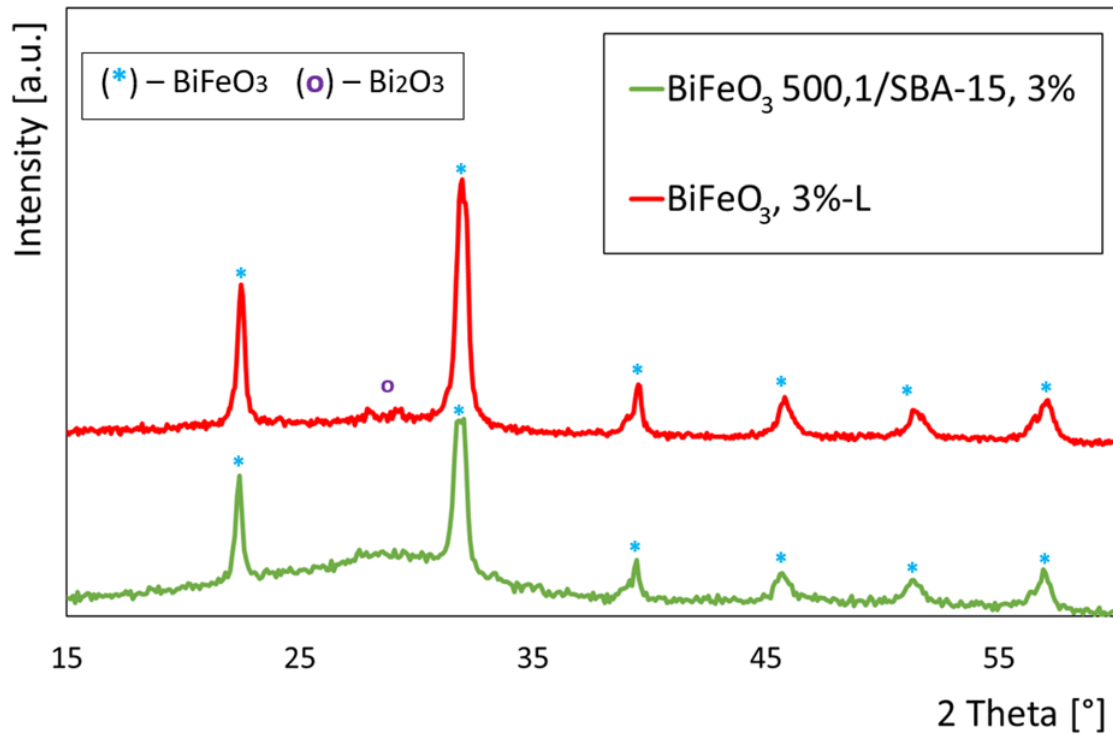


Figure 10. X-Ray diffractograms of BiFeO₃, 3% before and after leaching.

The crystallite size of the nanoparticles was determined for the BiFeO₃-0, 3% sample from Figure 7 and for the BiFeO₃, 3%-L leached sample from Figure 10 using the Scherrer equation.

$$D = \frac{0.9\lambda}{\beta \cos \theta} \quad (9)$$

where D is the crystallite size, λ is equal to 1.5418 Å (radiation wavelength), and β is the full width at half maximum (FWHM) for the diffraction angle 2θ . The peaks at $2\theta = 22.5^\circ$ for both samples were used for this propose. The results shown that when the Bi_{1.03}FeO₃ sample was not synthesized in the silica matrix the average nanoparticles size is of 30 nm, but when the nano-casting technique was applied, the average nanoparticles size decreased to 14 nm.

3.1.3. Transmission Electron Microscopy

TEM images of the BiFeO₃, 3% sample were analyzed by TEM to further investigate the particle size/distribution and morphology (see Figure 9). The BiFeO₃, 3% sample shows agglomerated particles with a nearly round shape of approximately 32 nm which is in accordance with the results obtained by the Scherrer equation. The TEM image for the BiFeO₃, 3%-L leached sample shows a relatively large particle size distribution between from 7.82 nm to 40.87 nm with most particles having a diameter <20nm. The larger particles are most probable residual NaOH due to insufficient H₂O washing after the leaching process. Alternatively, particle growth outside the pores of SBA15 due to excess precursor material or insufficient impregnation time due to an upscaling of the reaction (triple amount of the common quantity of precursors were used) could explain those larger particles. In general, the results obtained by TEM confirm the trend of the particles sizes obtained by XRD data analysis.

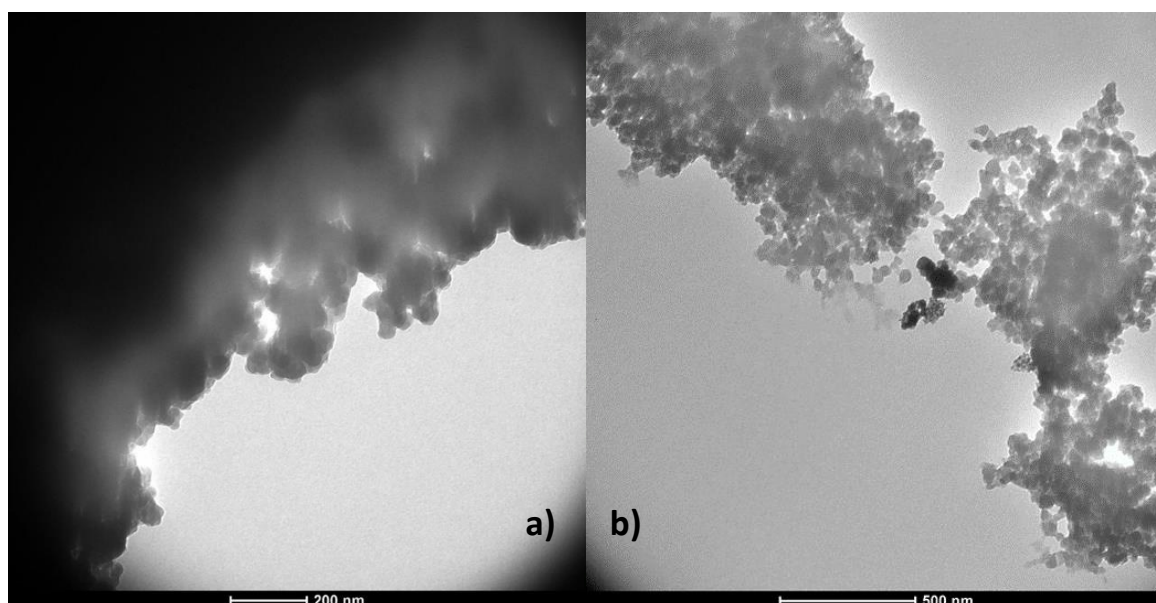


Figure 11. a) TEM images of sample BiFeO₃-0, 3% (left) and **b)** BiFeO₃, 3%-L leached (right).

3.2. UV-vis Absorption Spectroscopy

The optical properties of the BiFeO₃, 3%-L sample was analyzed by UV-vis diffuse reflection spectroscopy in order to obtain the bandgap value. To obtain this value, a transformation using the Kubelka-Munk method was carried out (Kubelka and Munk, 1931). To calculate the energy bandgap of the NPs it is necessary to graph a tangent line from the plot of the square root of Kubelka–Munk function with respect to the photon energy. As shown in the inset of Figure 12, the resulting bandgap energy is estimated about 2.05 eV. This low bandgap correlates very well to the small particle size observed by XRD and TEM (Bhunia, et al., 2013, Soltani, and Entezari, 2013).

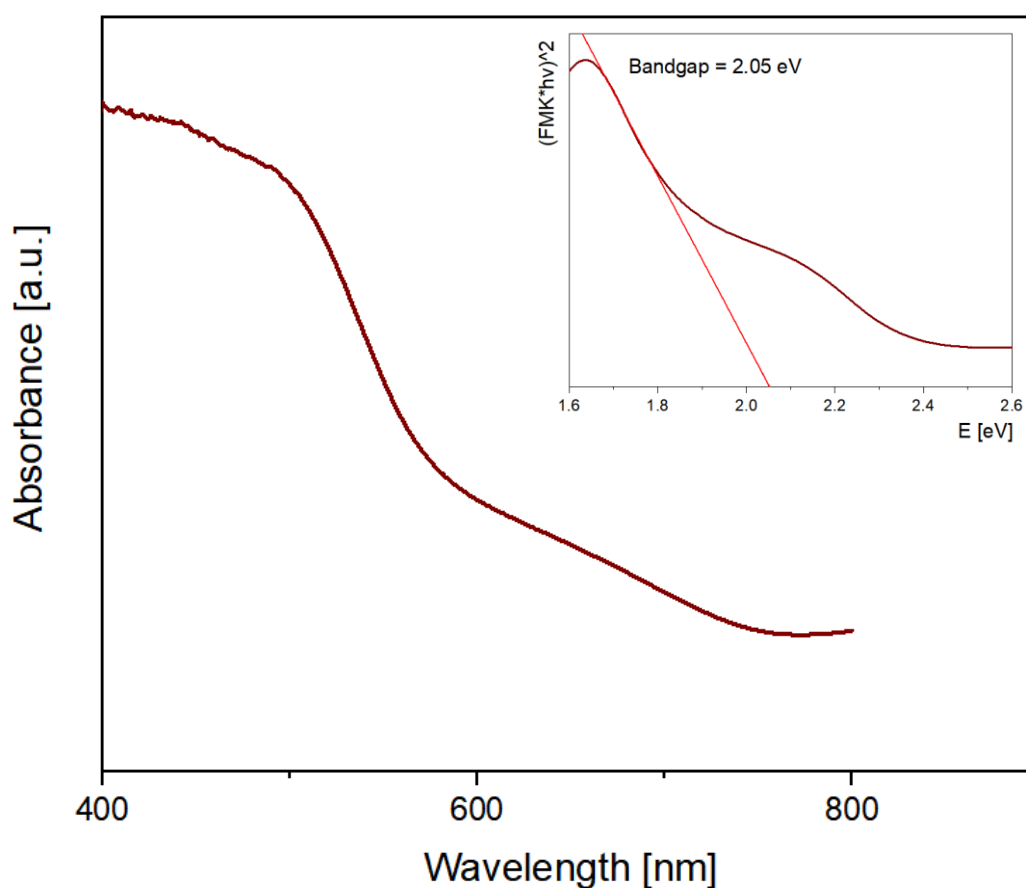


Figure 12. UV-vis spectrum of BiFeO₃, 3%-L, the inset shows bandgap plot for BiFeO₃, 3%-L nanoparticles.

3.3. Photocatalytic activity

The photocatalytic activity of the synthesized samples was evaluated using RhB model as organic pollutant and the sample, BiFeO₃, 2%, BiFeO₃ 500,1@SBA-15, 2% and BiFeO₃, 3%-L as the photocatalysts (Reddy, Shekar and Park, 2018). The stability of RhB had been previously evaluated under visible-light irradiation without the presence of photocatalysts, showing that is extremely stable and only degrades very slowly (Reddy, Shekar, Park, 2018, Soltani, and Entezari, 2013).

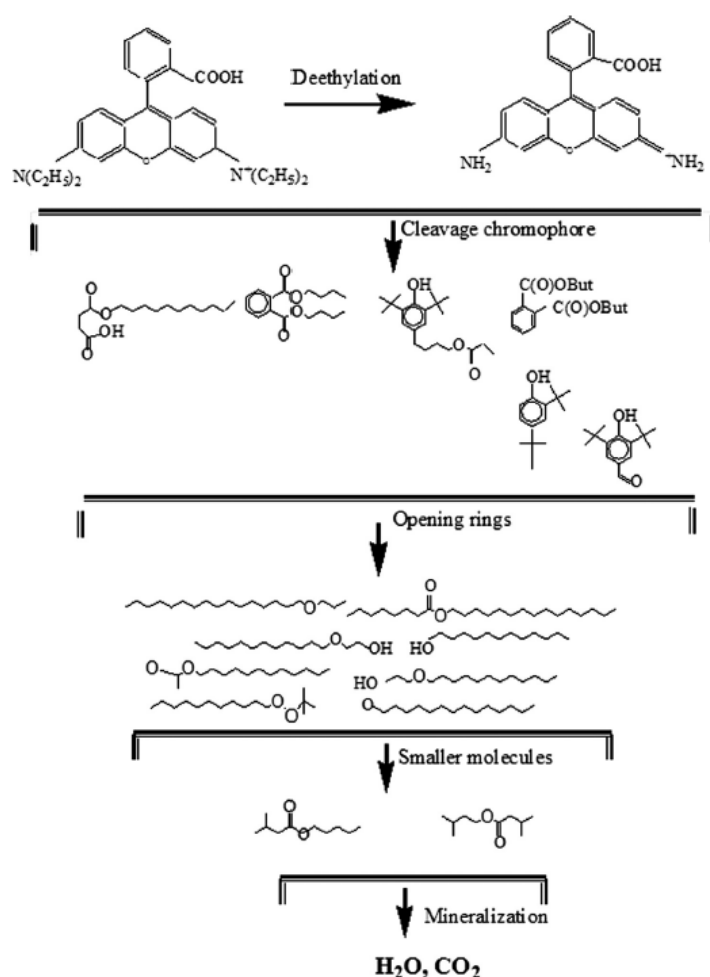


Figure 13. Mechanism of the photocatalytic degradation of RhB (Soltani, and Entezari, 2013, Merka, et al, 2011).

In order to establish an adsorption-desorption equilibrium between the catalyst and the RhB solution the reaction mixture was stirred for 1 hour, then the reactor

was turned on. Clearly, a photodegradation of RhB was observed under visible light irradiation by a notable decrease in its absorbance peak intensity at 553 nm. In addition, a shift of the absorption peak from 553 nm to lower wavelengths was also noticed, which indicates the formation of intermediate species based on the N-de-ethylation mechanism that leads to a direct degradation of the chromophore (Soltani, and Entezari, 2013, Merka, et al, 2011).

Figure 14 shows a typical decrease of the mentioned RhB peak intensity. For this photodegradation BiFeO₃, 3%-L leached nanoparticles were used at a pH 3, which shows an overall degradation of 93% of the RhB in a period of 240 min. Furthermore, the color change of the initial and final color of the sample can be visibly identified (see Figure 14).

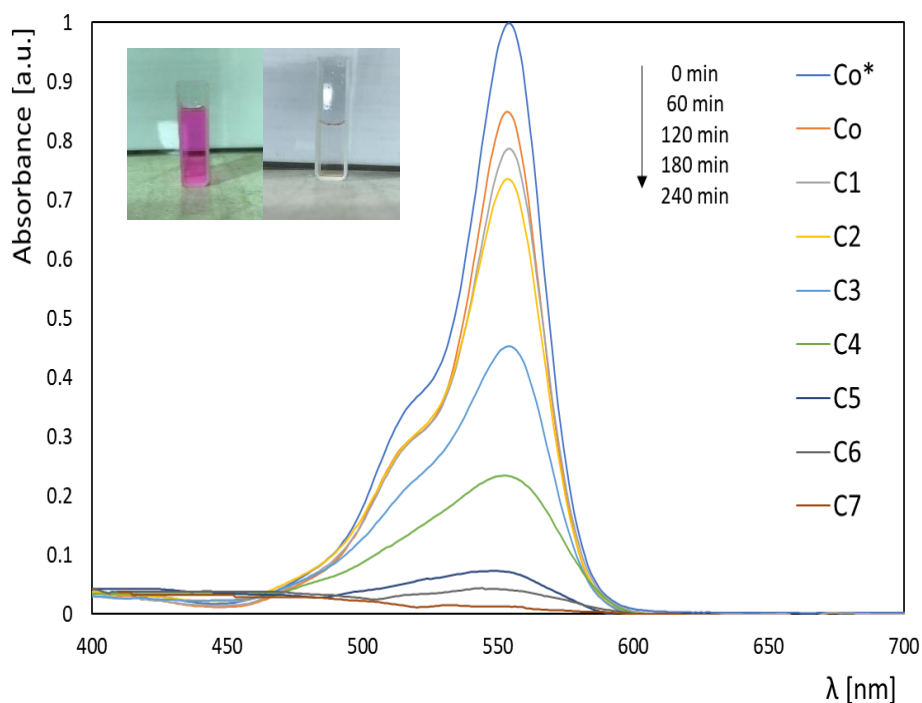


Figure 14. UV-vis spectra of RhB in dependence of irradiation time on BiFeO₃, 3%-L leached nanoparticles at pH 3, the inset is the color change of RhB for the first and last sample.

In order to evaluate the photodegradation efficiency of RhB by the different catalysts synthesized in function of irradiation time, the maximum intensity ratio (C/C_0) of RhB absorption peak values were calculated, being C_0 the absorbance peak at $t = 0$ and C at $t = t$ (Reddy, Shekar, and Park, 2018). Furthermore, the kinetics of the photocatalytic degradation of RhB in the presence of the different BiFeO₃ nano-materials was based on the Langmuir-Hinshelwood model, Eq. (3) (Soltani, and Entezari, 2013).

$$r = -\frac{dC}{dt} = \frac{k_r KC}{1 + KC} \quad (10)$$

Where r ($\text{mgL}^{-1}\text{min}^{-1}$) is the reaction rate, k_r ($\text{mg L}^{-1} \text{min}^{-1}$) is the reaction rate constant, K (L min^{-1}) is the reactant adsorption coefficient, c (mg L^{-1}), and t (min) is the irradiation time. Therefore, assuming a very small concentration, Eq. (2) becomes in the following:

$$r = -\frac{dC}{dt} = -k_r KC = kC \quad (11)$$

This new k (min^{-1}) is the pseudo first-order rate constant. After resolving the differential equation presented in Eq. (4), the model becomes in the following:

$$\ln\left(\frac{C}{C_0}\right) = -kt \quad (12)$$

Eq. (5) was plotted versus time, which after a linearization it was possible to obtain the rate constant values from the linear equation of each experiment. Figure 15 shows that the degradation of RhB increases when the particle size decreases. The catalysts BiFeO₃ 500,1@SBA-15, 2% showed a higher efficiency degrading RhB, compared to the BiFeO₃, 2% of 63% versus 49%, which can be

explained due to an increase in the surface area when overall particle size is reduced as seen in Figure 11.b. It should be noted that using just SBA-15 as a catalyst did not lead to any degradation after reaching the adsorption-desorption equilibrium.

After removing the SiO₂ matrix, liberated BiFeO₃, 3%-L nanoparticles showed the highest degradation efficiency, which implies that by removing the silica matrix all active sites on the catalyst surface become available for the interaction and degradation of the organic pollutant rather than being unavailable due to interaction with the SiO₂ surface. Here, a 93% of RhB photocatalytic degradation within 4 hours can be seen when the average nanoparticles size is 14 nm.

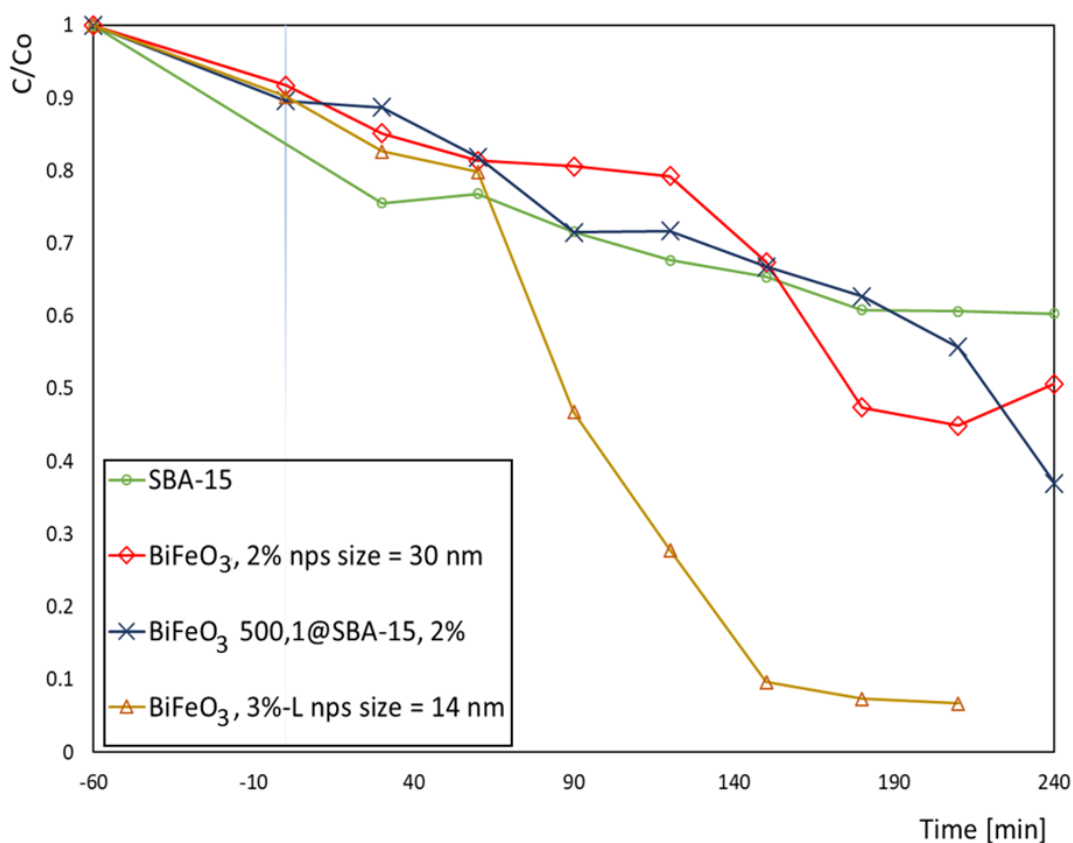


Figure 15. Photocatalytic degradation efficiency of RhB in presence of BiFeO₃ nano-materials.

Figure 16 shows the photocatalytic degradation kinetics of RhB in presence of different BiFeO₃ materials previously analyzed in function of time. Here, the highest degradation rate constant was observed for BiFeO₃, 3%-L leached nanoparticles.

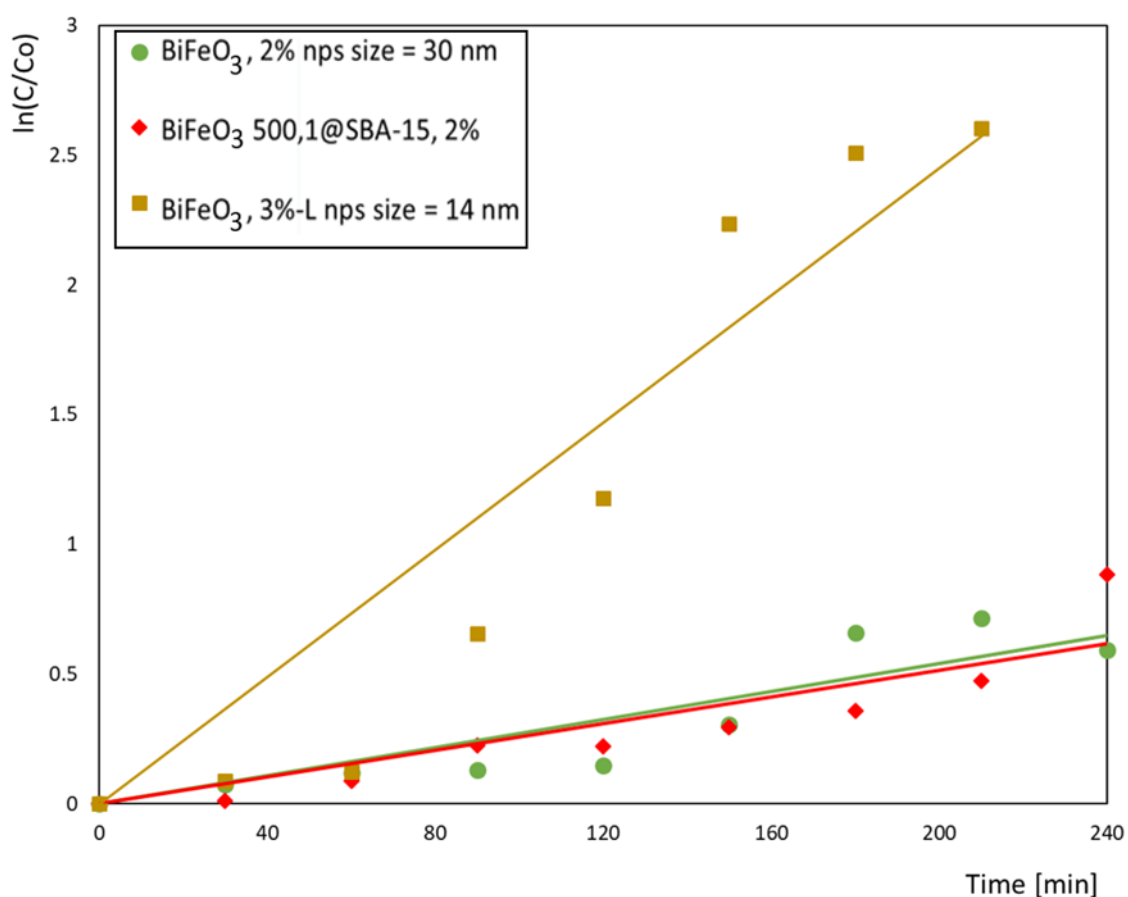


Figure 16. Photocatalytic degradation kinetics of RhB in presence of different BiFeO₃ nano-materials.

In Table 3. the rate constants of each sample are shown with the highest rate constant coming from the degradation using BiFeO₃, 3%-L with a nanoparticle size of 14 nm as a catalyst. The reactions order was determined to be pseudo-first order. However, the correlation coefficient suggests that the model does not fit well with the reaction kinetic. This behavior can be explained due to different

experimental errors in the photoreaction related to stirring, irradiation, beakers used, among others.

Table 3. Photodegradation kinetic parameters and degradation percentage of RhB in presence of different BiFeO₃ materials.

| Photocatalyst | Reaction | Rate | R ² | Total |
|---|------------------|--------------------------------------|----------------|--------------------|
| | order, n, [-] | constant, k, [min ⁻¹] | | Degradation [%] |
| BiFeO ₃ , 2% NPs size = ~30 nm | Pseudo 1st | 0.0027 | 0.8196 | 49 |
| BiFeO ₃ 500,1@SBA-15, 2% | Pseudo 1st | 0.0026 | 0.8151 | 63 |
| BiFeO ₃ , 3%-L NPs size = 14 nm | Pseudo 1st | 0.0123 | 0.8886 | 93 |

3.3.1. Photocatalytic activity after the reuse of BiFeO₃, 3%-L

The reusability of the catalyst was studied due to the importance for practical application. Here, a photodegradation of around 56% was observed for the first cycle. The relatively low degradation is explained by the high pH of 8.7 which is due to incomplete H₂O washing after the leaching process. It should be noted that higher pH values lead in general to a decrease in removal efficiency when using RhB as COO⁻ groups present in RhB at basic conditions, are repelled from the BiFeO₃ surface (Soltani and Entezari, 2013). Unfortunately, no degradation was observed after the 2nd cycle indicating no reusability of the catalyst using the current recovery method.

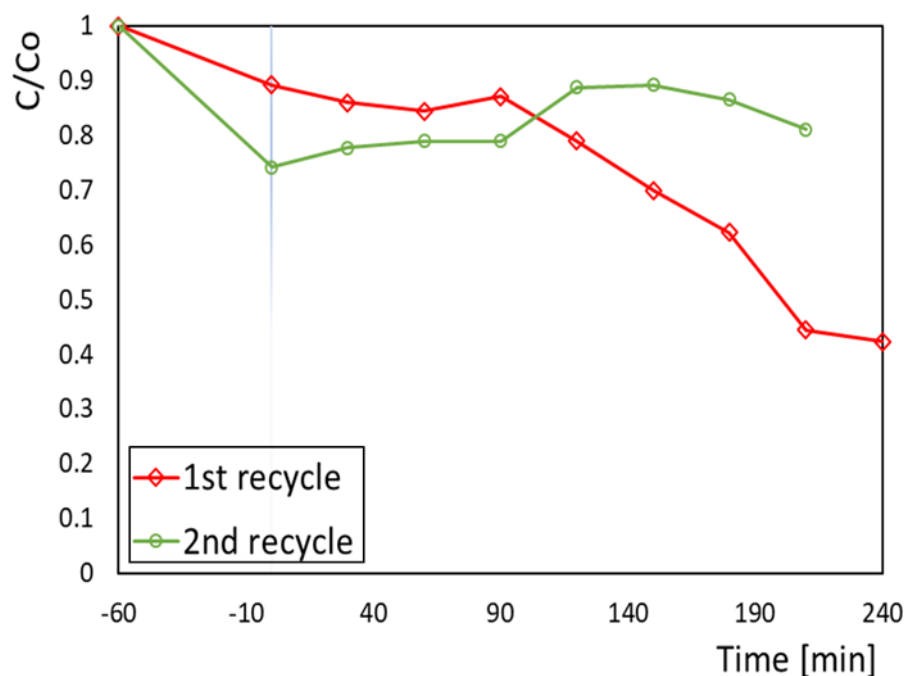


Figure 17. Photocatalytic degradation of RhB in two successive cycles on BiFeO₃, 3%-L leached nanoparticles.

In order to get an insight into the reusability problem infrared spectra of BiFeO₃, BiFeO₃ used at pH =2 and the recycled catalyst were recorded. In all cases an intense peak at approximately 560 cm⁻¹ can be observed due to bending vibrations of Fe-O bond which represents a fundamental absorption of FeO₆ octahedral in perovskite (Hasan, 2016). The most striking feature of the BiFeO₃ catalyst compared to the catalyst at pH =2 and the reused catalyst is a band at 1650 cm⁻¹ which corresponds to the ν_{asym} (C-O) of coordinated tartarate. This suggests that the tartaric acid degradation during the calcination was incomplete. At pH =2 the tartarate groups become replaced on the catalyst surface by nitrate groups as indicated by a disappearance of the peak at 1650 cm⁻¹ and the appearance of a nitrate peak at 1384 cm⁻¹ (symmetric stretching vibration bonds of N-O). These nitrate groups disappear upon the recycling procedure of the catalyst.

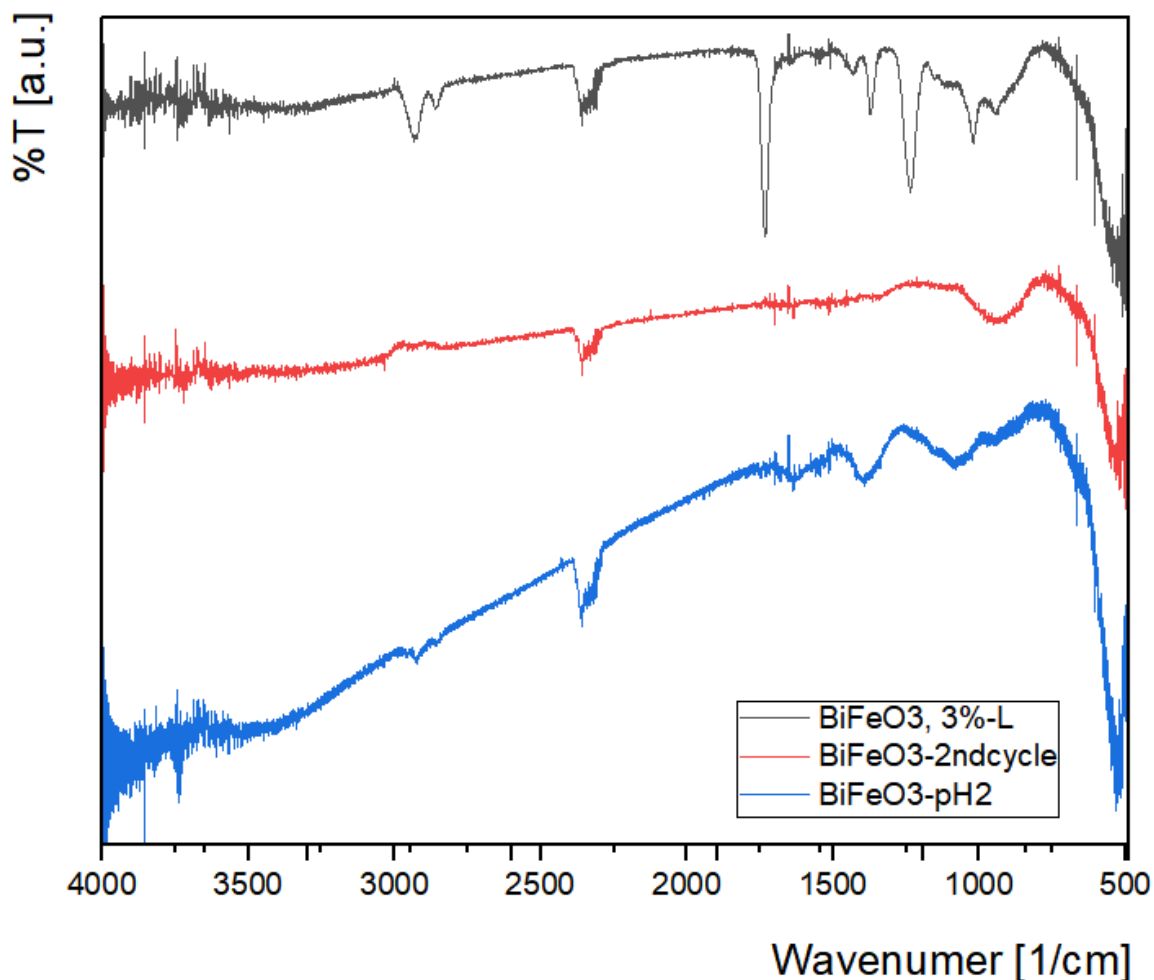


Figure 18. FT IR spectra of materials before and after being used for photocatalysis.

Higher drying temperature and longer drying times are required in order to reactivate the catalyst surface due to possible adsorption of residual dye fragments on the catalyst surface (Yu, et al., 2009).

3.3.2. Photocatalytic activity of BiFeO₃, 3%-L at different pH conditions

The degradation efficiencies of the RhB in the presence of BiFeO₃, 3%-L leached NPs at different pH were investigated as well. Figure 19 shows that a decrease in the pH affected positively to the photodegradation of RhB, where pH =2, showed 90% of degradation in less than 60 min and 98% degradation after 240 min.

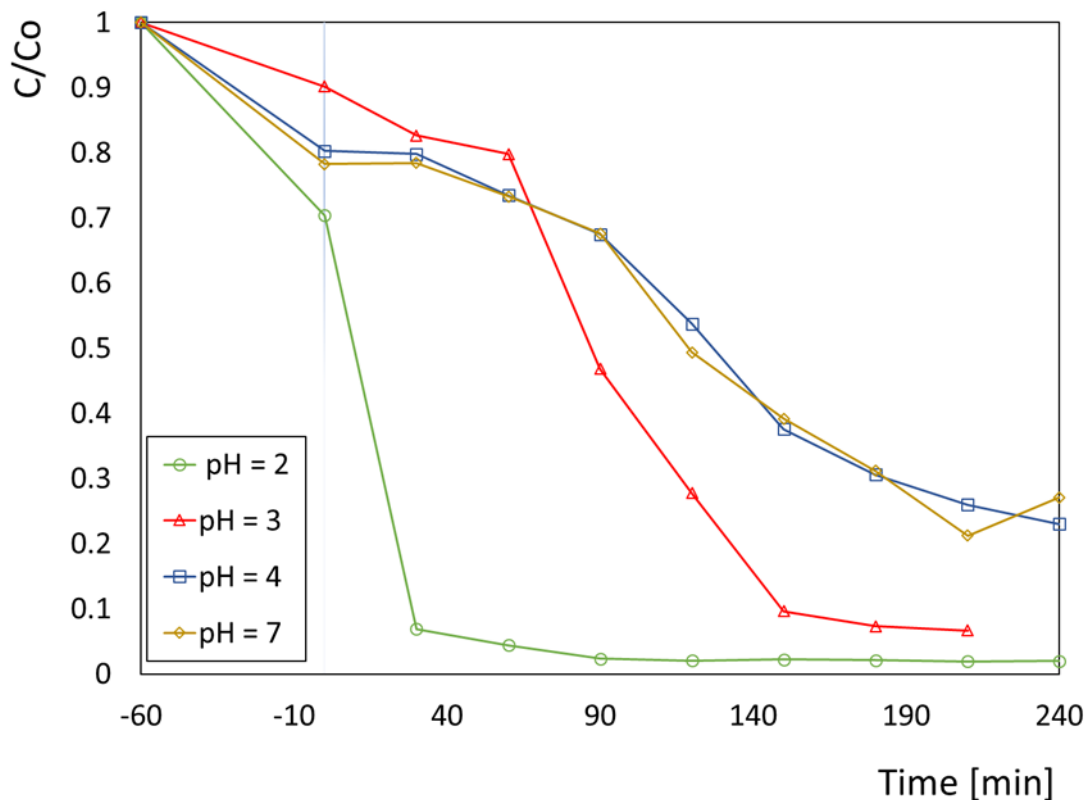


Figure 19. Photocatalytic degradation of RhB on BiFeO₃, 3%-L leached nanoparticles at different pH.

This increasing efficiency can be explained with surface-charge-properties. The molecule of RhB in solution possess ionic species that are interacting differently with the surface of the catalyst depending on the pH medium, thus promoting or hindering the degradation process.

Rhodamine B is composed by four N-ethyl groups at either side of the xanthere ring (Yu, et al., 2009). The aromatic carboxylic acid of the molecule has a pK_a around 4, which implies that at a pH medium lower than the pK_a value, protonation of the carboxyl group is favored as it can be seen in Figure 20. a (Soltani and Entezari, 2013). This will lead to an attractive interaction with the catalyst surface and this to a faster RhB degradation. On the other hand, at a pH medium higher than that pK_a value, the molecule will be favored in its

deprotonated form COO^- (see Figure 20. b). This leads the molecule to form a zwitterion, hybrid ion positively and negatively charged (Merka, et al, 2011). In this case, the deprotonated carboxyl group will have with a negative charge while the amino group is positively charged. This charge distribution leads primary to repulsive interactions with the catalyst surface. In addition, due to electrostatic interactions, dimers will be formed, making the molecule twice as large. This dimerization affects charge density throughout the molecule, possibly interfering in the degradation process (Soltani and Entezari, 2013).

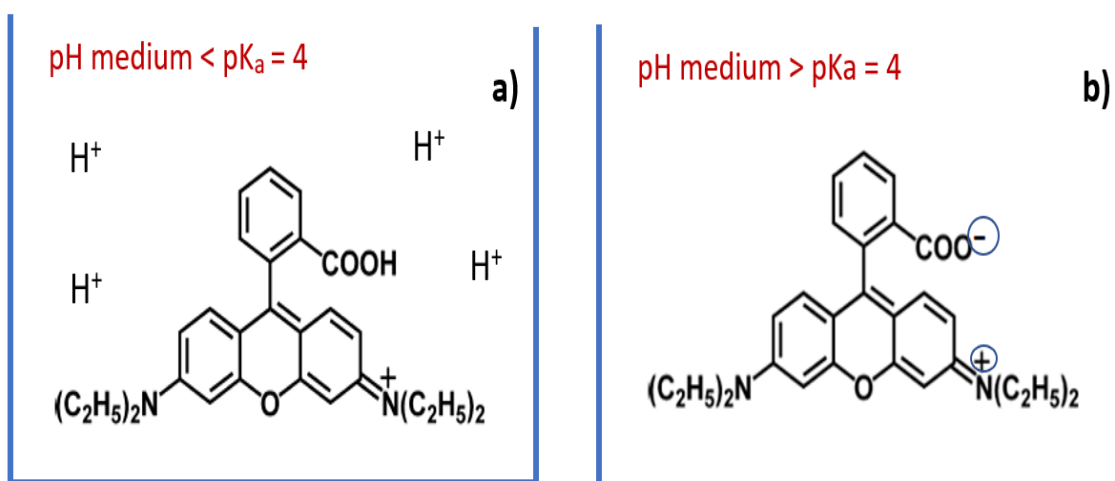


Figure 20. RhB molecule interactions according to the pH medium a) protonation of RhB, b) deprotonation of RhB, zwitterion formation.

Figure 21 shows the photocatalytic degradation kinetics of RhB in presence of BiFeO_3 , 3%-L leached NPs at different pH conditions. Here, the reactions follow a pseudo-first order as before and the highest degradation rate constants were observed at $\text{pH} > 4$.

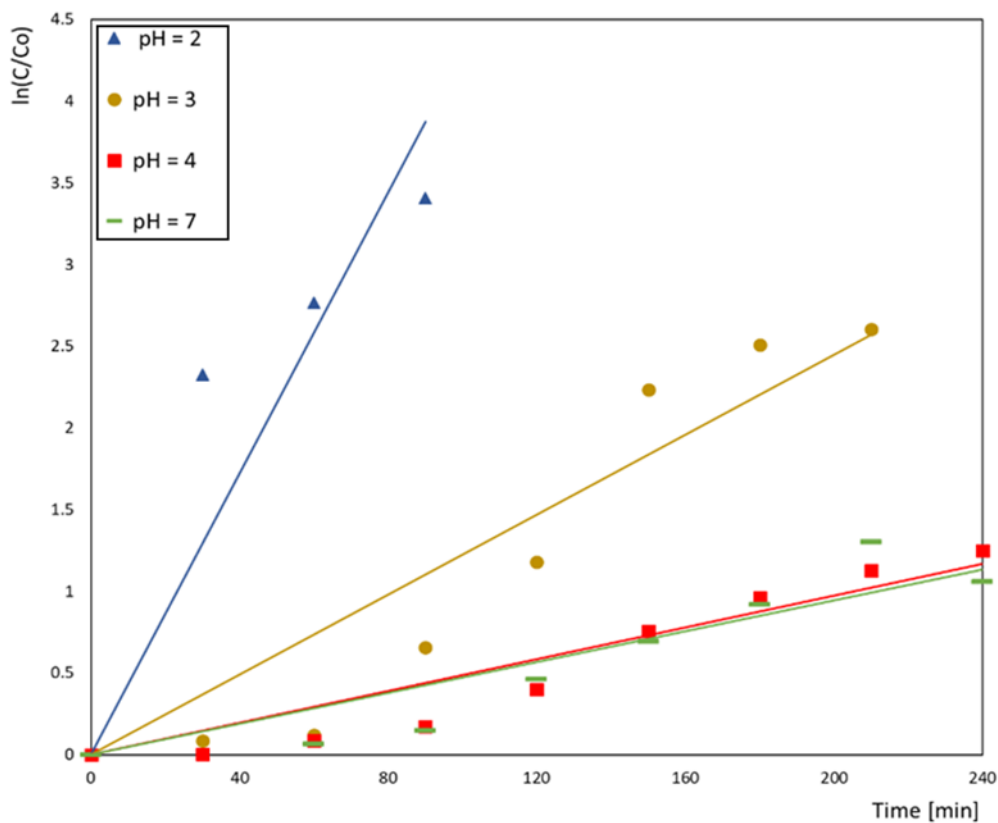


Figure 21. Photocatalytic degradation kinetics of RhB in presence of BiFeO₃, 3%-L leached nanoparticles at different pH.

Table 4 shows the summary of the kinetic parameters and the degradation efficiency under various pH values. As mentioned above, pH 2 represents an optimal value for the degradation of Rhodamine B showing the highest rate constant of 0.0431 min⁻¹, and a degradation efficiency of 100%.

Table 4. Photodegradation kinetic parameters and degradation percentage of RhB in presence of BiFeO₃ liberated nanoparticles at different pH.

| pH reaction | Reaction order, n, [-] | Rate constant, k, [min ⁻¹] | R ² | Total Degradation [%] |
|-------------|------------------------|--|----------------|-----------------------|
| 2 | Pseudo 1 st | 0.0431 | 0.8007 | 98 |
| 3 | Pseudo 1 st | 0.0123 | 0.8886 | 93 |
| 4 | Pseudo 1 st | 0.0049 | 0.9049 | 77 |
| 7 | Pseudo 1 st | 0.0047 | 0.8668 | 73 |

4. Conclusion

The present study describes the design, synthesis and application of highly crystalline BiFeO₃ nanoparticles by a nano-casting wet impregnation method using SBA-15 acting as hard template. It was shown that using tartaric acid as a complex ligand and acidified 2-methoxyethanol as a solvent and a 3% excess of Bi is essential to obtain the desired material. Furthermore, calcinations conditions show to be strongly correlated to the formation of this material. Here, intermediate plateaus and a final low calcination temperature of 500°C proved to be necessary in order to avoid the formation of unwanted phases such as Bi₂O₃ and Bi₂₅FeO₄₀.

Once the nanoparticles from the nano-casting technique were removed from the silica matrix a minor impurity of 1.7% Bi₂O₃ was visible. Furthermore, the nano-casting technique showed to be effective reducing the average nanoparticles to about 14 nm, compared to the average nanoparticles size of 30 nm obtained

without using SBA-15 as hard template. Those values were confirmed from the TEM analyses in agreement with XRD data using the Scherrer. The bandgap value of the BiFeO₃ leached nanoparticles of 2.05 eV also correlates very well with the particle size analysis. The photocatalytic activity was confirmed by degrading 93% of Rhodamine B during 4 hours for the liberated nanoparticles vs. 63% for the hosted nanoparticles, implying that in the BiFeO₃ leached nanoparticles more active sites are available for reacting with RhB. The kinetics of the photoreaction between RhB and BiFeO₃ shows to be of pseudo first order, based on the Langmuir–Hinshelwood model. The principle RhB degradation mechanism suggested an N-de-ethylation process which leads to a direct degradation of its chromophore.

After analyzing the photodegradation of RhB at different pH conditions it was possible to optimize the photodegradation reaction. Here, at a pH of 2 a degradation of 98% of RhB with reaction constant of 0.0431 min⁻¹ was observed.

References

- Bai, X., et al. (2016). Size Effect on Optical and Photocatalytic Properties in BiFeO₃ Nanoparticles. *The Journal of Physical Chemistry C*, 120 (7), 3595–3601.
- Bhunia, M., et al. (2013). Fine Dispersion of BiFeO₃ Nanocrystallites Over Highly Ordered Mesoporous Silica Material and Its Photocatalytic Property. *Journal of Nanoscience and Nanotechnology*, 13, 2557–2565.
- Deng, X., Chen, K. and Tüysüz, H. (2016). A Protocol for the Nanocasting Method: Preparation of Ordered Mesoporous Metal Oxides. *Chemistry of Materials*, 29 (1), 40–52.
- Gao, F., et al. (2006). Preparation and photoabsorption characterization of BiFeO₃ nanowires. *Appl. Phys. Lett*, 89 102506, doi: 10.1063/1.2345825
- Ghaly, A., et al. (2014). Production, Characterization and Treatment of Textile Effluents: A Critical Review. *J Chem Eng Process Technol* 5: 182. doi:10.4172/2157-7048.1000182
- Guo, R., et al. (2010). Enhanced Photocatalytic Activity and Ferromagnetism in Gd Doped BiFeO₃ Nanoparticles. *J. Phys. Chem*, 114 (49), 21390-21396.
- Hasan, M., et al. (2016). A soft chemical route to the synthesis of BiFeO₃ nanoparticles with enhanced magnetization. *Materials Research Bulletin*, 73, 179-186.
- He, J., et al. (2013). Characterization and visible light photocatalytic mechanism of size-controlled BiFeO₃ nanoparticles. *Materials Research Bulletin*, 48, 3017-3024.

- Huang, C., et al. (2010). Adsorption of cationic dyes onto mesoporous silica. *Microporous and Mesoporous Materials*, 141, 102-109.
- Ishii, Y., et al. (2013). Pore Size Determination in Ordered Mesoporous Materials using Powder X-ray diffraction. *The Journal of Physical Chemistry*, 117 (35), 18120–18130.
- Kant, R. (2012). Textile Dyeing Industry and Environmental Hazard. *Natural Science*, 4(1), 22-26. doi:10.4236/ns.2012.41004
- Kubelka, P., & Munk, F. (1931). A contribution to the appearance of the Paint. *Journal of Technical Physics*, 12, 593-601.
- Lam, S., Sin, J. and Rahman, A. (2017). A newly emerging visible light-responsive BiFeO₃ perovskite for photocatalytic applications: A mini review. *Materials Research Bulletin*, 90, 15-30.
- Lotey, G. S. and Verma, N. K. (2013). Synthesis and characterization of BiFeO₃ nanowires and their applications in dye-sensitized solar cells. *Materials Science in Semiconductor Processing*, doi: 10.1016/j.mssp.2013.11.029i
- Ma, J., Quiang, L and Xue, J. (2013). Effect of Different Calcination Temperatures on the Structural and Photocatalytic Performance of Bi-TiO₂/SBA-15. *International Journal of Photoenergy*, doi: 10.1155/2013/875456
- Merka, O., et al (2011). pH-Control of the Photocatalytic Degradation Mechanism of Rhodamine B over Pb₃Nb₄O₁₃. *J. Phys. Chem. C* 2011, 115, 8014–8023.
- Nair, M., Kaliaguine, S. and Kleitz, F. (2014). Nanocast mesoporous mixed metal oxides for catalytic application. *Comptes Rendus Chimie*, 17, 641-655.

- Papadas, I. (2013). Templated Assembly of BiFeO₃ Nanocrystals into 3D Mesoporous Networks for Catalytic Applications. *Nanoscale*, doi: 10.1039/x0xx00000x
- Papadas, I., et al. (2014). A high surface area ordered mesoporous BiFeO₃ semiconductor with efficient water oxidation activity. *Journal of Materials Chemistry A*, 2015 (3), 1587-1593.
- Papadas, I., et al. (2016). Templated Self-Assembly of Colloidal Nanocrystals into 3D Mesoscopic Structures: A Perspective on the Synthesis and Catalytic Prospects. *Chemistry of Materials*, 28 (9), 2886–2896.
- Pattnaik, S., et al. (2018). Synthesis, photoelectrochemical properties and solar light-induced photocatalytic activity of bismuth ferrite nanoparticles. *J Nanopart Res*, 20:10, doi: 10.1007/s11051-017-4110-5
- Ponraj, C, Vinitha, G. and Daniel, J. (2017). A review on the visible light active BiFeO₃ nanostructures as suitable photocatalyst in the degradation of different textile dyes. *Environmental Nanotechnology, Monitoring and Management*, 7, 110-120.
- Quickel, T. E., et al. (2015). Mesoporous bismuth ferrite with amplified magnetoelectric coupling and electric field-induced ferrimagnetism. *NATURE COMMUNICATIONS*, doi: 10.1038/ncomms7562
- Quiñonez, J., et al. (2013). Easy Synthesis of High-Purity BiFeO₃ Nanoparticles: New Insights Derived from the Structural, Optical, and Magnetic Characterization. *Inorganic Chemistry* (2013) 52 (18), 10306-10317.

- Reddy, B., Rajendar, V. and Park, M. (2018). Particle size effects on the photocatalytic activity of BiFeO₃ particles. *Digest Journal of Nanomaterials and Biostructures*, 13 (1), 87-95.
- Reza, K., Kurny, A. and Gulshan, F. (2017). Parameters affecting the photocatalytic degradation of dyes using TiO₂: a review. *Applied Water Sciece*, 7 (1), 1569-1578.
- Santillán, P. (2017). Synthesis of Porous BiFeO₃ Materials and Their Application in Water Treatment Reactions. (Tesis de pregrado). Universidad San Francisco de Quito. Quito. Ecuador.
- Soltani, T. and Entezari, M. (2013). Sono-synthesis of bismuth ferrite nanoparticles with high photocatalytic activity in degradation of Rhodamine B under solar light irradiation. *Chemical Engineering Journal*, 223, 145-154.
- Srinivasan, N., et al. (2015). Photocatalysis by morphologically tailored mesoporous silica (SBA-15) embedded with SnO₂nanoparticles: Experiments and model. *Applied Catalysis A: General*, 498, 107-116.
- UNESCO. (2017). World Water Day 2017. Retrieved from <http://www.unesco.org/new/en/unesco/events/prizes-and-celebrations/celebrations/international-days/world-water-day-2017/>
- World Health Organization. (2018). Drinking-water. Retrieved from <https://www.who.int/news-room/fact-sheets/detail/drinking-water>

Yu, K., et al. (2009). Visible Light-Driven Photocatalytic Degradation of Rhodamine B over NaBiO₃: Pathways and Mechanism. *J. Phys. Chem*, 113 (37), 10024-10032.

Zhang, N., et al. (2016). Enhanced visible Light Photocatalytic Activity of Gd-doped BiFeO₃ Nanoparticles and Mechanism in sight. *Nature*. doi:10.1038/srep26467

Appendix



Figure 22.a. Solution of RhB mixed with BiFeO₃ under visible light irradiation.

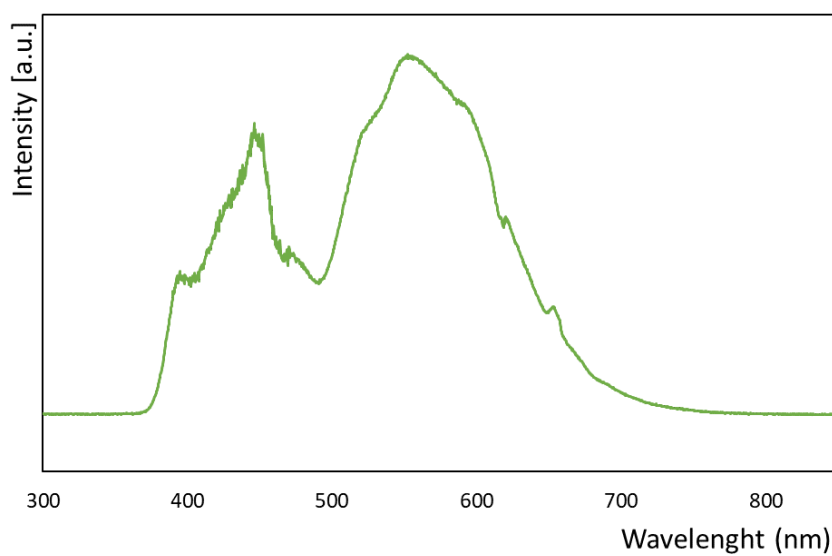


Figure 23.a. Wavelength spectra of the photoreactor used to simulate the visible light.

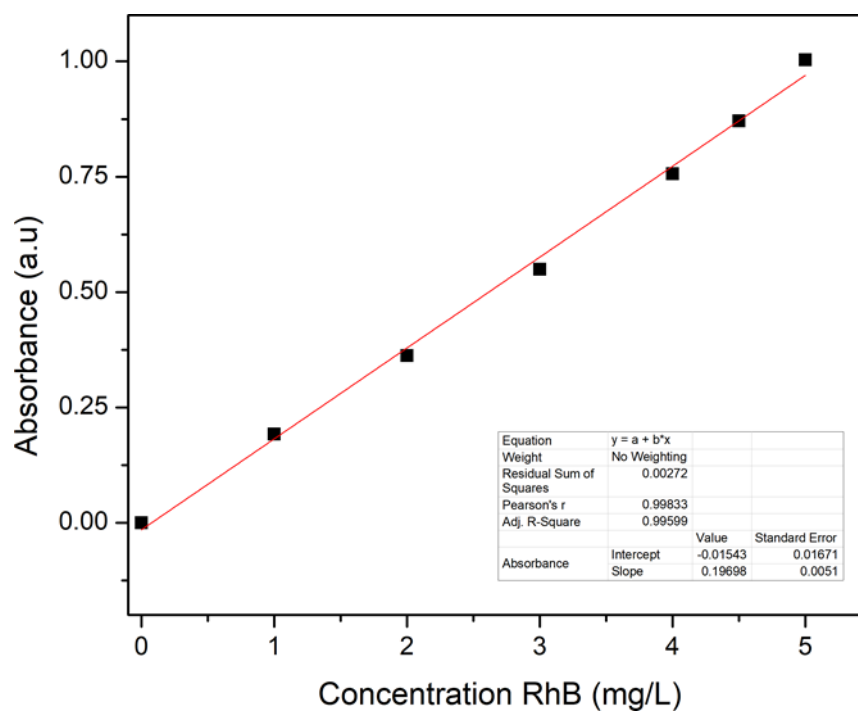


Figure 24.a. Calibration curve of RhB applied to calculate the concentration of RhB.

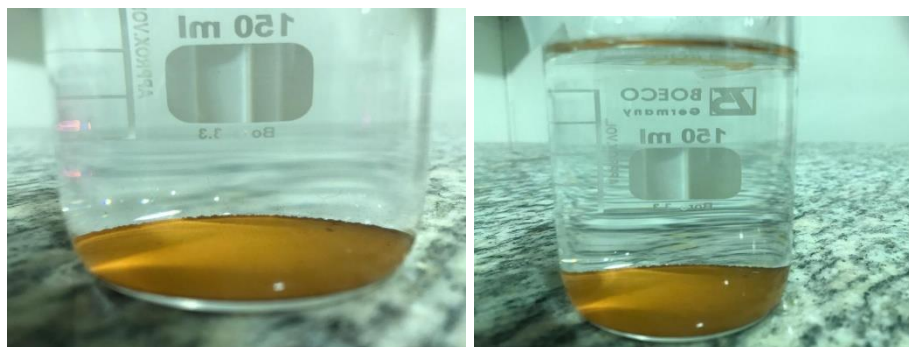


Figure 25. a. Color of the solution after the photodegradation of RhB with $\text{Bi}_{1.03}\text{FeO}_3$ leached nanoparticles at pH 2.



Figure 26. a. Bi_{1.03}FeO₃ leached nanoparticles catalyst.